The Astrophysical Journal, 888:93 (20pp), 2020 January 10 https://doi.org/10.3847/1538-4357/ab5d37

Time-varying Extinction, Polarization, and Colors of Type Ia Supernovae due to Rotational Disruption of Dust Grains

Nguyen Chau Giang[1], Thiem Hoang[2,3], and Le Ngoc Tram[1,4]
[1] University of Science and Technology of Hanoi, VAST, 18 Hoang Quoc Viet, Vietnam
[2] Korea Astronomy and Space Science Institute, Daejeon 34055, Republic of Korea; thiemhoang@kasi.re.kr
[3] Korea University of Science and Technology, 217 Gajeong-ro, Yuseong-gu, Daejeon 34113, Republic of Korea
[4] SOFIA-USRA, NASA Ames Research Center, MS 232-11, Moffett Field, CA 94035, USA
Received 2019 July 10; revised 2019 November 15; accepted 2019 November 27; published 2020 January 13

Abstract

Observations toward type Ia supernovae (SNe Ia) frequently report an unusually low total-to-selective extinction ratio ($R_V < 2$) and a small peak wavelength of polarization ($\lambda_{max} < 0.4\,\mu$m). Hoang et al. proposed that the dominance of small grains near SNe Ia due to RAdiative Torque Disruption (RATD) can explain the puzzle. To test this scenario, we model the dust extinction and polarization of SNe Ia, accounting for grain disruption and alignment by radiative torques and different grain tensile strengths from $S_{max} = 10^7$–10^{10} erg cm^{-3}. We find that R_V decreases from ∼3.1 to ∼1.5 after disruption time $t_{disr} < 40$ days for clouds at a distance $d < 4$ pc from SNe Ia. We then calculate the observed lightcurves of SNe Ia and find that their colors change with time, due to varying dust extinction. The peak wavelength λ_{max} also decreases from ∼0.55 to ∼0.15 μm over an alignment time of $t_{align} < 10$ days, due to the enhanced alignment of small grains. By fitting the theoretical polarization with the Serkowski law characterized by the K and λ_{max} parameters, we find that K increases when large grains are disrupted by RATD, which is consistent with the unusual K versus λ_{max} relationship of SNe Ia. Nevertheless, an accurate measurement of K and λ_{max} is challenging, due to atmospheric effects and potential contamination of polarization by Rayleigh scattering by circumstellar matter. Our results demonstrate the importance of RATD for time-dependent extinction, polarization, and colors of SNe Ia.

Unified Astronomy Thesaurus concepts: Astrosphere interstellar medium interactions (106); Interstellar dust (836); Interstellar dust extinction (837); Interstellar dust processes (838); Type Ia supernovae (1728); Supernovae (1668); Core-collapse supernovae (304); Starlight polarization (1571)

1. Introduction

A Type Ia supernova (hereafter SN Ia) is the explosion of a white dwarf star in a binary system, wherein the accretion of material from the evolving companion star onto the white dwarf increases the white dwarf's mass to ∼1.4 $M_\odot$, i.e., the Chandrasekhar limit (Hillebrandt & Niemeyer 2000). Beyond this mass limit, the electron degeneracy pressure is insufficient to support the white dwarf against gravity, and the white dwarf collapses, releasing a large amount of material and energy into the surrounding environment. SNe Ia have similar intrinsic luminosities because they explode at similar masses; as such, SNe Ia are considered "standard candles" for measuring cosmological distances (Riess et al. 1998). SNe Ia are also useful for studying the physical and chemical properties of the interstellar medium (ISM) of external galaxies (Nobili & Goobar 2008; Foley et al. 2014; Brown et al. 2015).

Dust grains along the line of sight toward SNe Ia absorb, scatter, and polarize the SN radiation in the ultraviolet–near-infrared (UV–NIR) wavelength range (see, e.g., Hoang 2017). Photometric observations of SNe Ia show that the total-to-selective extinction ratio $R_V = A_V/E(B-V)$, with A_V the optical extinction and $E(B-V) = A_B - A_V$ the color excess, is much lower than the standard value of interstellar dust in the Milky Way, which is $R_V \sim 3.1$. For example, 80 SNe Ia studied by Nobili & Goobar (2008) have an average value of $R_V \sim 1.75$. Using the *Hubble Space Telescope* and the *Swift* satellite, Amanullah et al. (2015) and Wang et al. (2012) estimated a range of $R_V \sim 1.4$–3. These examples can be explained by the peculiar properties of dust in the SN Ia's host galaxy. Other suggestions include the scattering of circumstellar (CS) material in the vicinity of SNe Ia (Goobar 2008; Wang et al. 2008) and the enhancement of small grains (smaller than 0.05 μm) relative to large grains (size above 0.1 μm) in the local interstellar environment of SNe Ia (Phillips et al. 2013; Hoang 2017).

Moreover, polarimetric observations of SNe Ia also reveal an unusually low value of the wavelength at the maximum polarization curve (hereafter peak wavelength), with $\lambda_{max} < 0.4\,\mu$m, which is much lower than the standard value of the ISM of $\lambda_{max} = 0.55\,\mu$m (Whittet et al. 1992). For instance, four SNe Ia (1986G, 2006X, 2008fp, and 2014J) show $\lambda_{max} \sim$ 0.05–0.43 μm (Kawabata et al. 2014; Patat et al. 2015; Hoang 2017), and nine SNe Ia considered in Zelaya et al. (2017) have $\lambda_{max} < 0.4\,\mu$m. Based on a simultaneous fitting to the extinction and polarization curves of SNe Ia, Hoang (2017) found that the unusual values of λ_{max} can be reproduced if small grains can be aligned as efficiently as large ones.

The enhancement in the abundance of small grains relative to large ones around SNe Ia is the popular explanation for the anomalous values of R_V and λ_{max} (Hoang 2017). The remaining question is why there is such a predominance of small grains near SNe Ia. Subject to intense radiation fields, dust grains are known to be destroyed via thermal sublimation, but this mechanism only destroys grains within a small radius of $R_{sub} \simeq 0.015(L_{UV}/10^9\,L_\odot)^{1/2}(T_{sub}/1800\,\mathrm{K})^{-2.8}$ pc, where L_{UV} is the total luminosity of SNe Ia in the NUV–optical band and T_{sub} is the grain sublimation temperature (Waxman & Draine 2000; Hoang et al. 2019). Grain shattering by grain–grain collisions can enhance the abundance of small grains, but

this process takes ~100 yr if grains are accelerated by radiation pressure to relativistic velocities of $v \sim 0.028c$. However, the values of R_V and λ_{max} are measured during the early-time observations (less than a few weeks after the explosion). Thus, the reason why small grains are predominant around SNe Ia remains mysterious.

The mystery of the predominance of small grains around SNe Ia seems to have been resolved when Hoang et al. (2019) introduced a new mechanism of grain destruction, the so-called RAdiative Torque Disruption (RATD), which is based on the centrifugal force within rapidly spinning grains spun up by radiative torques (RATs). This RATD mechanism can break a large grain into small fragments on a characteristic timescale of tens of days, which results in the variation of the grain-size distribution over time. The first goal of this paper is, therefore, to model the time-dependent extinction and polarization of SNe Ia due to dust grains being disrupted by RATD. We will demonstrate that RATD can indeed reproduce the low values of R_V and λ_{max} observed toward SNe Ia.

Intrinsic colors and lightcurves of SNe Ia are crucially important for achieving an accurate measurement of the cosmological constant and better constraints of dark energy, which are considered the next frontiers in SN Ia cosmology. However, a major systematic uncertainty lies in the uncertainty of dust extinction toward SNe Ia (see, e.g., Scolnic et al. 2019). Moreover, intrinsic lightcurves are essential for understanding the trigger mechanism of SNe Ia. The second goal of this paper is thus to quantify the time variation of SN Ia colors due to time-varying extinction caused by RATD.

The structure of this paper is as follows. In Section 2, we review the RATD mechanism and calculate the disruption size of dust grains as functions of time and cloud distance toward SNe Ia. In Sections 3 and 4, we will model the dust extinction and polarization curves induced by grains aligned with the magnetic fields using the grain-size distribution determined by RATD and the grain-alignment function from RAT alignment theory. In Section 5, we will predict the observed lightcurves of SNe Ia, which vary with time due to RATD. An extended discussion and a summary of our main findings are presented in Sections 6 and 7, respectively.

2. Rotational Disruption of Dust Grains by SN Ia Light

2.1. The RATD Mechanism

When dust grains of irregular shapes are illuminated by an intense radiation field, such as that around SNe Ia, RATs induced by the interaction of anisotropic radiation with the irregular grain can spin the grain up to extremely fast rotation (Draine & Weingartner 1996; Lazarian & Hoang 2007; Hoang et al. 2019). Such a suprathermal rotation of grains produces high centrifugal stress that can exceed the maximum tensile strength of grain material, such that grains are disrupted into small fragments (Hoang et al. 2019). This RATD mechanism was described in detail in Hoang et al. (2019). In the following, we briefly describe the RATD mechanism for reference. Note that the grain shape must be irregular to experience RATs, but we can approximate it as a spherical grain of effective size a, which has the same volume as the irregular one (see, e.g., Draine & Weingartner 1996; Lazarian & Hoang 2007).

The luminosity of SNe Ia varies over time, which can be approximately described by an analytical formula (Zheng et al. 2017):

$$L_{\rm SN\,Ia}(t) = L_0\left(\frac{t-t_0}{t_p}\right)^{\alpha_r}\left[1+\left(\frac{t-t_0}{t_p}\right)^{s\alpha_d}\right]^{-2/s}, \quad (1)$$

where L_0 is the scaling parameter, and we take $L_0 = 2\times10^{10}L_\odot$. The first term describes the rising luminosity of SNe Ia (Riess et al. 1999), while the second term describes the decrease of the luminosity after the peak around at time t_p. We take $\alpha_r = 2$, $\alpha_d = 2.5$, $s = 1$, $t_0 = 0$ days, and $t_p = 23$ days (Hoang et al. 2019).

Because the luminosity of SNe Ia is time dependent, the grain angular velocity can only be obtained by numerically solving the equation of motion (see Hoang et al. 2019),

$$\frac{Id\omega}{dt} = \Gamma_{\rm RAT} - \frac{I\omega}{\tau_{\rm damp}}, \quad (2)$$

where I is the grain inertia moment with $I = 8\pi\rho a^5/15$ and ρ the grain mass density, $\Gamma_{\rm RAT}$ is the radiative torque, and $\tau_{\rm damp}$ is the characteristic timescale of grain rotational damping.

Usually, one needs to average $\Gamma_{\rm RAT}$ over the radiation spectrum, and the averaged RAT is given by

$$\Gamma_{\rm RAT} = \pi a^2\gamma u_{\rm rad}\left(\frac{\bar\lambda}{2\pi}\right)\overline{Q}_\Gamma, \quad (3)$$

where πa^2 is the geometric cross section, γ is the anisotropy degree of the radiation field ($0\leqslant\gamma\leqslant1$), $\bar\lambda$ is the mean wavelength of the radiation spectrum, and $\overline{Q}_\Gamma$ is the averaged RAT efficiency. Here, $u_{\rm rad} = \int u_\lambda d\lambda$ with u_λ the spectral energy density is the radiation energy density of the radiation field at distance d from the source as given by

$$u_{\rm rad} = \frac{L_{\rm bol}e^{-\tau}}{4\pi cd^2}, \quad (4)$$

where τ is the effective optical depth defined by $e^{-\tau} = \int u_\lambda\times e^{-\tau_\lambda}d\lambda/u_{\rm rad}$, which describes the extinction of SN light by intervening dust. Let $U = u_{\rm rad}/u_{\rm ISRF}$, where $u_{\rm ISRF} = 8.64\times10^{-13}\,{\rm erg\,cm^{-3}}$ is the energy density of the average interstellar radiation field (ISRF) in the solar neighborhood (see Hoang et al. 2019).

In general, Q_Γ depends on the grain size and shape, the wavelength, and the angle between the direction of the grain's maximum moment of inertia axis and the incident radiation (Lazarian & Hoang 2007; Herranen et al. 2019). When the anisotropic radiation direction is parallel to the axis of the maximum moment of inertia, Lazarian & Hoang (2007) found that Q_Γ can be approximated by a power law:

$$\bar{Q}_\Gamma = \begin{cases} \approx 2\left(\dfrac{\bar\lambda}{a}\right)^{-2.7} & \text{for } a \lesssim a_{\rm trans} \\ \approx 0.4 & \text{for } a > a_{\rm trans}, \end{cases} \quad (5)$$

where $a_{\rm trans} = \bar\lambda/1.8$ (see also Hoang & Lazarian 2008 and Hoang & Lazarian 2014).

The damping of grain rotation can arise from collisions with gas species (atoms and molecules) followed by thermal evaporation. Reemission of infrared radiation also causes the damping of grain rotation. Thus, the total damping rate can be

written as (Hoang et al. 2019)

$$\tau_{\rm damp} = \frac{\tau_{\rm gas}}{1 + F_{\rm IR}}, \quad (6)$$

where $\tau_{\rm gas}$ is the rotational damping timescale due to collisions given by

$$\tau_{\rm gas} \simeq 8.74 \times 10^4 a_{-5}\hat{\rho}\left(\frac{30\ {\rm cm}^{-3}}{n_{\rm H}}\right)\left(\frac{100\ {\rm K}}{T_{\rm gas}}\right)^{1/2}\ {\rm yr}, \quad (7)$$

with $a_{-5} = a/(10^{-5}\,{\rm cm})$ and $\hat{\rho} = \rho/3\ {\rm g\ cm}^{-3}$, $n_{\rm H}$ the gas density, and $T_{\rm gas}$ the gas temperature (see Draine & Weingartner 1996; Hoang & Lazarian 2009), and $F_{\rm IR}$ describes the damping by IR emission.

Assuming that grains are in thermal equilibrium between radiative heating and cooling by infrared emission, the IR damping coefficient can be estimated as (see Draine & Lazarian 1998)

$$F_{\rm IR} \simeq \frac{0.4U^{2/3}}{a_{-5}}\frac{30\ {\rm cm}^{-3}}{n_{\rm H}}\left(\frac{100\ {\rm K}}{T_{\rm gas}}\right)^{1/2}. \quad (8)$$

A spinning grain of angular velocity ω is disrupted when the centrifugal stress $S = \rho a^2\omega^2/4$ exceeds the maximum tensile strength of grain material $S_{\rm max}$ (Hoang et al. 2019). The critical angular velocity at which the disruption occurs is determined by $S \equiv S_{\rm max}$, which yields

$$\omega_{\rm disr} = \frac{2}{a}\left(\frac{S_{\rm max}}{\rho}\right)^{1/2}, \quad (9)$$

where $S_{\rm max}$ depends on the grain internal structure and composition. Compact grains are expected to have higher $S_{\rm max}$ than composite grains. For instance, polycrystalline bulk solid can have $S_{\rm max} \sim 10^9$–10^{10} erg cm^{-3} (Burke & Silk 1974; Draine & Salpeter 1979), while ideal materials, i.e., diamond, have $S_{\rm max} \sim 10^{11}$ erg cm^{-3} (see Hoang et al. 2019). These high values are likely suitable for small grains, i.e., nanoparticles, due to their compact structure. In contrast, large grains of $a \gtrsim 0.1\ \mu$m) likely have a composite structure, such that the tensile strength is lower of $S_{\rm max} \sim 10^6$–10^8 erg cm^{-3} (Hoang 2019). Therefore, in this paper, we consider a wide range of tensile strength and adopt $S_{\rm max} = 10^7$ erg cm^{-3} as a typical strength for our discussion unless stated otherwise.

The characteristic timescale of grain disruption by RATD is estimated as

$$t_{\rm disr} = \frac{I\omega_{\rm disr}}{dJ/dt} = \frac{I\omega_{\rm disr}}{\Gamma_{\rm RAT}} \simeq 38(\gamma U_6)^{-1}\bar{\lambda}_{0.5}^{1.7}\hat{\rho}^{1/2}S_{\rm max,7}^{1/2}a_{-5}^{-0.7}\ {\rm days} \quad (10)$$

for $a_{\rm disr} < a \lesssim a_{\rm trans}$, and

$$t_{\rm disr} \simeq 2.5(\gamma U_6)^{-1}\bar{\lambda}_{0.5}^{-1}\hat{\rho}^{1/2}S_{\rm max,7}^{1/2}a_{-5}^{2}\ {\rm days} \quad (11)$$

for $a > a_{\rm trans}$, where $\bar{\lambda}_{0.5} = \bar{\lambda}/(0.5\mu m)$, $U_6 = U/10^6$, and $S_{\rm max,7} = S_{\rm max}/(10^7\ {\rm erg\ cm}^{-3})$.

For our calculations, we assume a dust model including two separate populations of silicate and carbonaceous grains (Mathis et al. 1977; Li & Draine 2001). We assume that carbonaceous grains of size $\geqslant$50 Å, which are primarily responsible for the extinction and polarization of starlight from UV–NIR wavelengths, have graphitic properties. Therefore, in this paper, we use the term "graphite" to represent the carbonaceous grains. Other dust materials such as SiC can have high tensile strength if they have a compact structure, but this dust population is a minor component of the interstellar dust (Whittet et al. 1990). Assuming the mass density $\rho = 3.5$ and 2.2 g cm^{-3} for silicate and graphite materials, one can see that the disruption time of graphite grains is shorter than that of silicate grains due to its lower mass density.

2.2. Grain Disruption Sizes

The critical size of the grain disruption by the RATD mechanism depends on the tensile strength of the grain material $S_{\rm max}$, the strength of the radiation field U that is determined by the cloud distance to SNe Ia, the radiation spectrum, and the irradiation time. As in Hoang et al. (2019), SNe Ia are considered to be a blackbody radiation source with an effective temperature of $T_\star = 15,000$ K. This yields the mean wavelength of $\bar{\lambda} \approx 0.35\ \mu$m. We assume that the radiation field is unidirectional, i.e., $\gamma = 1$.

We solve Equation (2) numerically to obtain $\omega_{\rm RAT}(t)$ for a grid of grain sizes a and compare it with $\omega_{\rm disr}(a)$ (Equation (9)) to determine the grain disruption size $a_{\rm disr}$ and the disruption time $t_{\rm disr}$ (see Hoang et al. 2019 for details).

Figure 1 (upper panel) shows the variation of grain disruption size with the cloud distance at $t = 15$, 30, 45, and 60 days, assuming a typical tensile strength $S_{\rm max} = 10^7$ erg cm^{-3} and the typical gas density $n_{\rm H} = 30$ cm^{-3}. For distant clouds ($d >$ 3.5 pc), grain disruption cannot occur because the radiation energy density is insufficient to spin up large grains to the critical limit. For this case, we set $a_{\rm disr} = 0.25\ \mu$m, which is the popular upper cutoff of the grain-size distribution of interstellar dust (Mathis et al. 1977). As the cloud distance decreases, the grain disruption size decreases rapidly because the radiation strength increases as $U \propto d^{-2}$. Moreover, within 15 days, only grains within $d \sim 1.5$ pc can be disrupted, and after 60 days, even grains located at $d \sim 3$ pc can be disrupted because of longer irradiation time.

Figure 1 (lower panel) shows the variation of the grain disruption size with time for the different cloud distances. For a given distance, the disruption size starts to decrease rapidly with time from the original value after the disruption time $t_{\rm disr}$, and it achieves a saturated value when the disruption ceases. Dust grains closer to SNe Ia receive higher radiation energy density and require shorter irradiation to disrupt (i.e., smaller $t_{\rm disr}$). As a result, one can see that the decrease of $a_{\rm disr}$ begins earlier, but its saturation also ends earlier than grains at farther distances. For example, from Figure 1 (lower panel), one can obtain $t_{\rm disr} \sim 6$, 10, 19, and 34 days for silicate grains at $d = 0.5$, 1, 2, and 3 pc, respectively (see more details in Figure 3 in Hoang et al. 2019). The decrease of $a_{\rm disr}$ starts from $t \sim t_{\rm disr}$ and achieves saturation of $a_{\rm disr} \sim 0.01$–$0.03\ \mu$m. We note that for all cloud distances considered in Figure 1, grain disruption ceases after about 60 days because the SN luminosity already decreases substantially after its peak.

Figure 2 (upper panel) shows the disruption size of silicate grains as a function of the cloud distance for different $S_{\rm max}$. Grains with a lower tensile strength can be disrupted out to a larger distance than those with higher $S_{\rm max}$. This can be seen from Equation (9), where grains with higher $S_{\rm max}$ have a higher critical angular velocity and require a higher radiation energy (i.e., smaller distance) to be disrupted. For example, for a dust cloud at 1 pc, the disruption size $a_{\rm disr} \sim 0.009\ \mu$m for

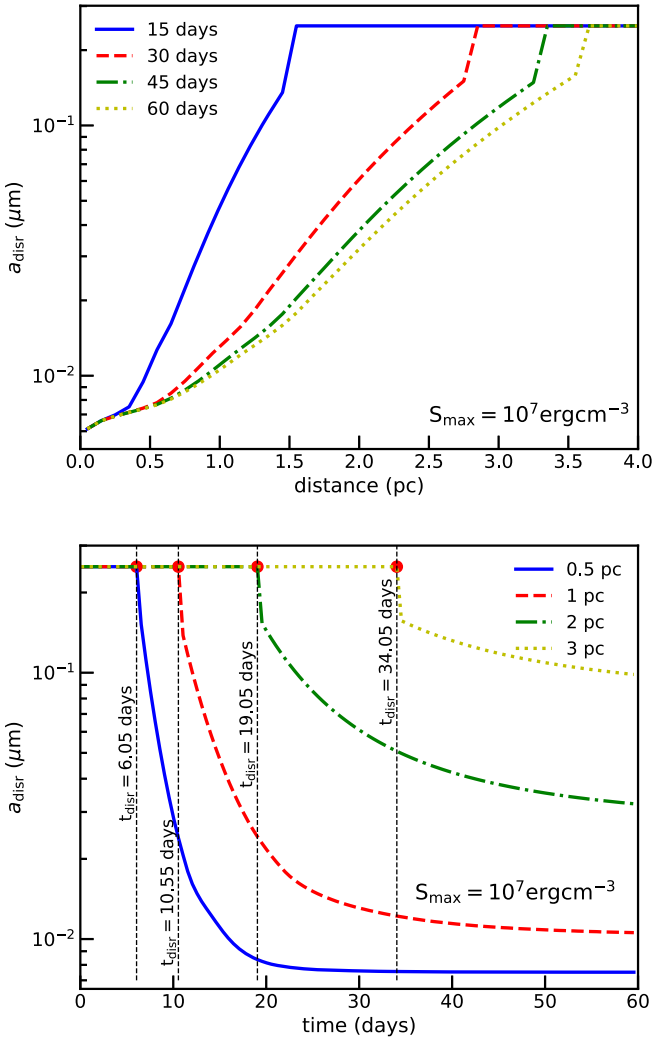

Figure 1. Upper panel: disruption size of silicate grains as a function of cloud distance evaluated at 15, 30, 45, and 60 days, assuming the tensile strength $S_{max} = 10^7$ erg cm^{-3}. Lower panel: disruption size of silicate vs. time for the dust cloud located between 0.5 and 3 pc. The disruption size starts to decrease from an original value of 0.25 μm after some disruption time t_{disr} marked by the vertical dotted line.

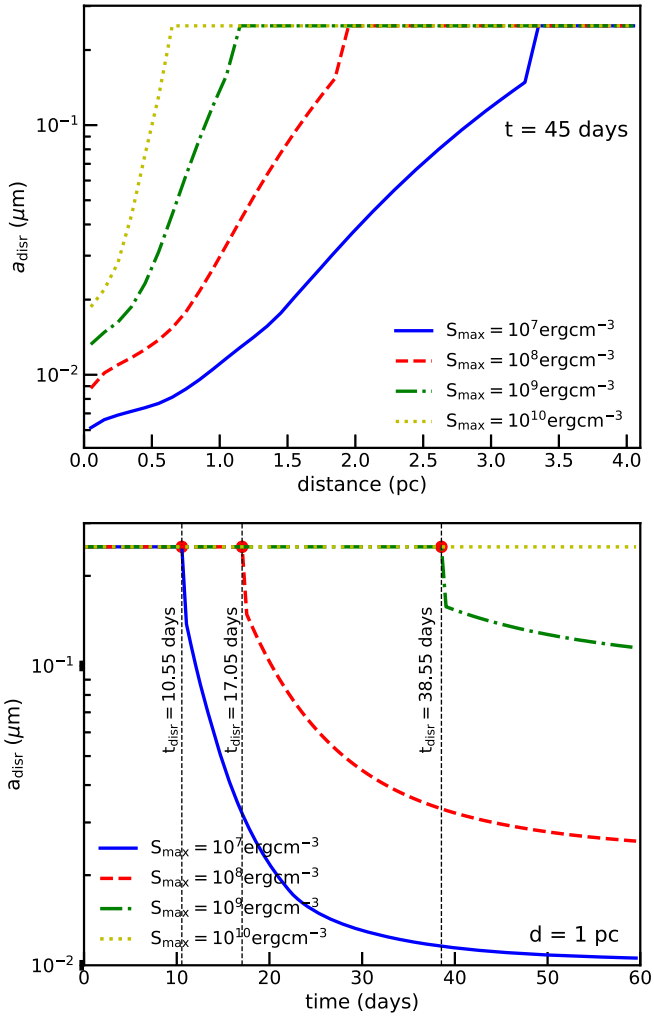

Figure 2. Disruption size of silicate vs. cloud distance evaluated at 45 days (upper panel) and disruption size vs. time for clouds at 1 pc for different values of S_{max}. Vertical lines mark the disruption time by RATD.

$S_{max} = 10^7$ erg cm^{-3}, but it increases to $a_{disr} \sim 0.07$ μm for $S_{max} = 10^9$ erg cm^{-3}. There is no disruption for very strong materials of $S_{max} = 10^{10}$ erg cm^{-3}. Moreover, the active region of RATD, which is defined by the maximum distance D_{disr} that grains are still disrupted, is smaller when grains have higher maximum tensile strength. For example, the disruption distance decreases from $D_{disr} = 4$ pc for $S_{max} = 10^7$ erg cm^{-3} to $D_{disr} = 0.5$ pc for $S_{max} = 10^{10}$ erg cm^{-3}.

Figure 2 (lower panel) shows the disruption size of silicate grains as a function of time for a dust cloud at 1 pc for different S_{max}. The disruption time of grains with higher S_{max} is longer, and grain disruption stops earlier at a higher saturated grain size. For example, the disruption time is $t_{disr} \sim 10$, 17, and 38 days for $S_{max} = 10^7$, 10^8, and 10^9 erg cm^{-3}, respectively. The final disruption sizes are $a_{disr} \sim 0.01$, 0.03, and 0.1 μm for these tensile strengths.

We also calculated the grain disruption size for different gas densities $n_H \sim 10$–10^4 cm^{-3} and found that the disruption size is almost the same for clouds within 4 pc from the source. This arises from the fact that the intense radiation field of SNe Ia results in the dominance of IR damping over gas damping, i.e., $F_{IR} \gg 1$, so that n_H from τ_{gas} and F_{IR} are canceled out in Equation (6). As a result, the rotational damping rate τ_{damp} only depends on the radiation strength.

3. Extinction of SN Light in the Presence of the RATD Effect

3.1. Grain-Size Distribution

Usually, one describes the grain-size distribution by a power law:

$$\frac{dn^j}{da} = C_j n_H a^\alpha, \quad (12)$$

where j denotes the grain composition (silicate and graphite), C_j is the normalization constant, and α is the power slope.

For the standard ISM in our galaxy, Mathis et al. (1977) derived the slope $\alpha = -3.5$, $C_{sil} = 10^{-25.11}$ cm$^{2.5}$ for silicate grains, and $C_{gra} = 10^{-25.14}$ cm$^{2.5}$ for graphite grains. The size distribution has a lower cutoff of $a_{min} = 3.5$ Å determined by thermal sublimation due to temperature fluctuations of very small grains (see, e.g., Draine & Li 2007), and an upper cutoff of $a_{max} = 0.25$ μm (Mathis et al. 1977).

In the strong radiation field of SNe Ia, large grains are disrupted into smaller ones due to RATD, resulting in a decrease of $a_{\rm max}$. Therefore, we set $a_{\rm max} = a_{\rm disr}$. Because the dust mass is conserved in the RATD mechanism, the grain-size distribution dn/da must be modified.

Due to the lack of experimental study on the size distribution of the fragments resulting from rotational disruption, we will assume that the new grain-size distribution also follows a power law. One can think of three possible ways to model the size distribution of grains modified by RATD. First, the power slope should vary, but the normalization constant C is assumed to be fixed (model 1). Second, the slope is assumed to be fixed, but the normalization constant C varies (model 2). Third, both C and the slope should vary (model 3). Model 1 corresponds to the case in which the original large grains are made up of small constituents of various sizes. Model 2 corresponds to the case where an originally large grain is disrupted into smaller fragments that follow the same size distribution as the original one. Model 3 would require a detailed understanding of the internal structure of dust grains, which is uncertain and thus beyond the scope of this paper. So we consider here model 1 and will discuss its difference with model 2 in Appendix A.

For a given grain disruption size $a_{\rm disr}$, the new value of the size distribution slope is determined by the conservation of the dust mass:

$$\int_{a_{\rm min}}^{a_{\rm max}} a^3 C a^{-3.5} da = \int_{a_{\rm min}}^{a_{\rm disr}} a^3 C_{\rm new} a^{\alpha} da, \tag{13}$$

which yields

$$\frac{a_{\rm disr}^{4+\alpha} - a_{\rm min}^{4+\alpha}}{4+\alpha} = \frac{a_{\rm max}^{0.5} - a_{\rm min}^{0.5}}{0.5}. \tag{14}$$

The new slope α is obtained by numerically solving Equation (14). Note that the unit of the constant $C_{\rm new}$ must be changed accordingly to conform with the new slope α.

3.2. Extinction Curves

The radiation intensity of SNe Ia is reduced mainly due to the absorption and scattering (i.e., extinction) of dust along the line of sight. The extinction efficiency of light by a dust grain is defined by

$$Q_{\rm ext} = \frac{C_{\rm ext}}{S} = \frac{C_{\rm ext}}{\pi a^2}, \tag{15}$$

where $C_{\rm ext}$ is the extinction cross section. We use a mixed-dust model comprising silicate and graphite materials (Weingartner & Draine 2001; Draine & Li 2007) and take the $C_{\rm ext}$ calculated for oblate spheroidal grains of axial ratio $a/b = 2$ from Hoang et al. (2013).

The extinction of supernova light at wavelength λ in the unit of magnitude per atom is given by (see e.g., Hoang et al. 2013)

$$\frac{A(\lambda)}{N_{\rm H}} = \sum_{j={\rm sil,gra}} 1.086 \int_{a_{\rm min}}^{a_{\rm max}} C_{\rm ext}^{j}(a) \left(\frac{1}{n_{\rm H}} \frac{dn^j}{da}\right) da, \tag{16}$$

where the column density $N_{\rm H} = \int n_{\rm H} dz = n_{\rm H} L$, with L the path length, dn^j/da the grain-size distribution of dust component j, and $a_{\rm max} = a_{\rm disr}$.

For a given $a_{\rm disr}$, the new grain-size distribution is obtained, and we can calculate the wavelength-dependence extinction by dust being modified by RATD using Equation (16).

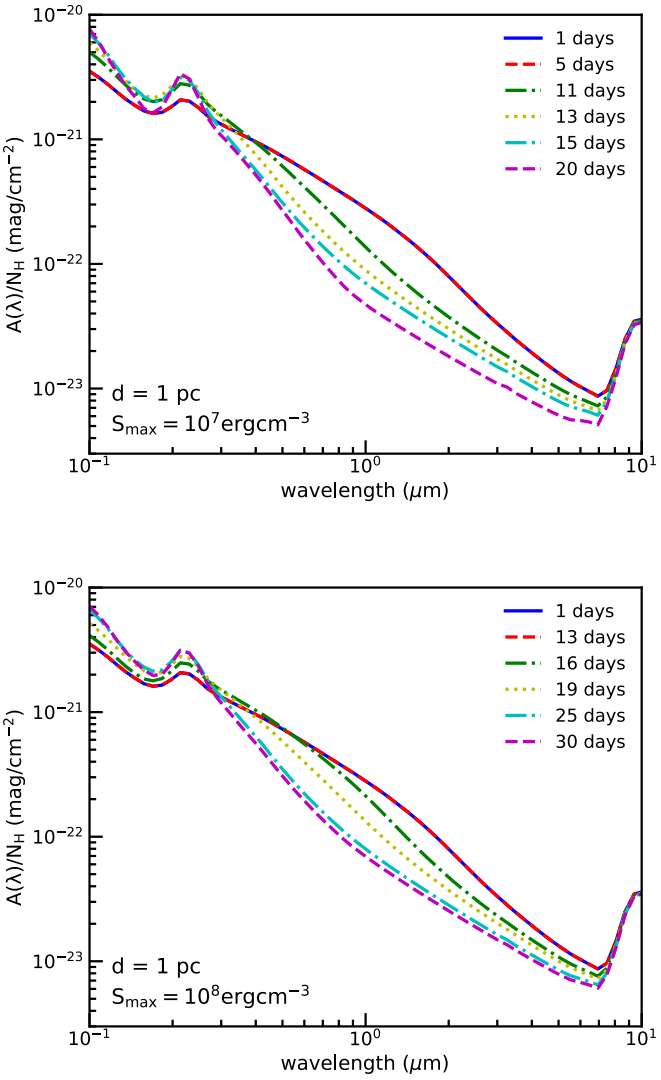

Figure 3. Extinction curves evaluated at different times for $S_{\rm max} = 10^7$ erg cm^{-3} (upper panel) and $S_{\rm max} = 10^8$ erg cm^{-3} (lower panel), assuming the dust cloud is 1 pc from SNe Ia. The extinction at $\lambda > 0.4$ μm decreases while the extinction at $\lambda < 0.4$ μm increases over time.

Figure 3 shows the extinction curves evaluated at different times for dust grains located at a distance $d = 1$ pc from the source and the maximum tensile strength $S_{\rm max} = 10^7$ erg cm^{-3} (upper panel) and $S_{\rm max} = 10^8$ erg cm^{-3} (lower panel). In the upper panel, the extinction curve at $t = 5$ days (red dashed line) is the same as the extinction at $t = 1$ days because $t < t_{\rm disr}$ (see Equation (10)). For $t > t_{\rm disr} \sim 10$ days (see Figure 1, lower panel), the optical–NIR extinction decreases rapidly with time due to the removal of large grains by RATD. On the other hand, the UV extinction is increased due to the enhancement in the abundance of small grains by RATD. The extinction at $\lambda > 7$ μm is essentially unchanged because the wavelength is much larger than the grain radius, i.e., $\lambda \gg (2\pi\ a)$.

The lower panel of Figure 3 shows the extinction curve for grains with $S_{\rm max} = 10^8$ erg cm^{-3}. The variation in the extinction curve with time is similar to the upper panel, but it starts later because of a larger disruption time with $t_{\rm disr} \sim 15$ days (see Figure 2, lower panel).

Figure 4 shows the extinction curves for the different cloud distances at $t = 45$ days, assuming $S_{\rm max} = 10^7$ erg cm^{-3} (upper

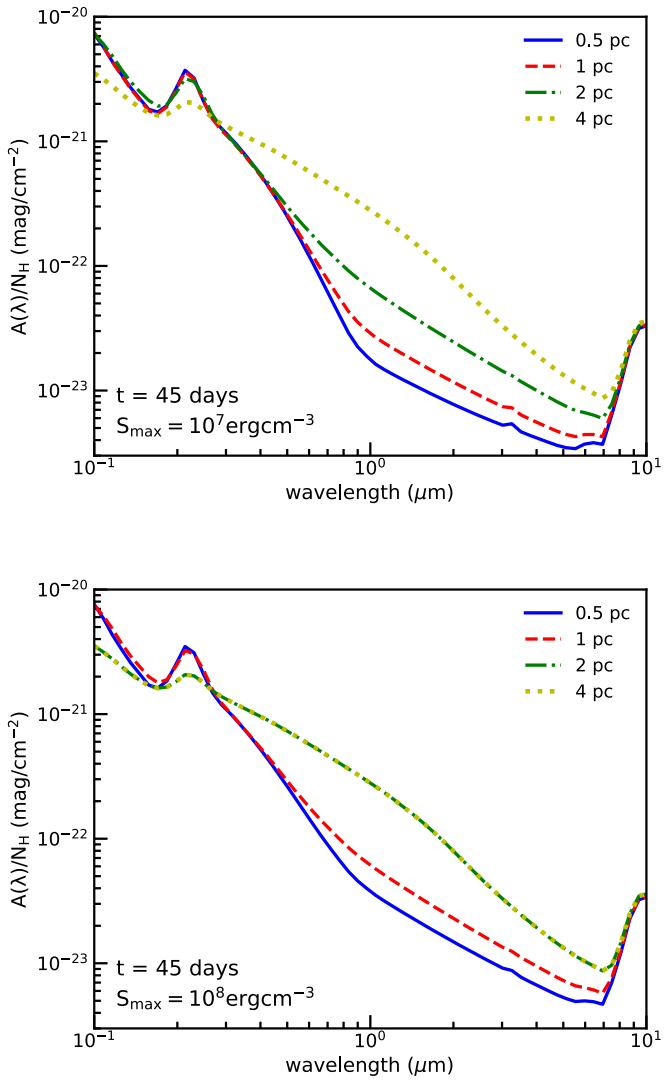

Figure 4. Extinction curve evaluated at $t = 45$ days for the different cloud distances $d = 0.5$, 1, 2, and 4 pc for $S_{max} = 10^7$ erg cm^{-3} (upper panel) and $S_{max} = 10^8$ erg cm^{-3} (lower panel). The extinction curve at $d = 4$ pc is closely similar to that of the original dust without RATD.

panel) and $S_{max} = 10^8$ erg cm^{-3} (lower panel). The optical–NIR extinction decreases while the NUV extinction increases with decreasing cloud distance. This is a direct consequence of the dependence of the grain disruption size on the cloud distance as shown in Figure 1.

Figure 5 shows the time dependence of the ratio $A(\lambda, t)/A(\lambda, 0)$ for the different photometric bands (FUV to R bands) and various cloud distances. Here we choose $\lambda = 0.15\,\mu$m for the far-UV band (FUV), $\lambda = 0.25\,\mu$m for the mid-UV band (MUV), and $\lambda = 0.3\,\mu$m for the near-UV band (NUV). As shown, the ratio $A(\lambda, t)/A(\lambda,0)$ is constant during the initial stage of $t < t_{disr}$ before grain disruption, and it starts to rapidly change when RATD begins at t_{disr}. For example, optical–NIR extinction (e.g., R band, black line) decreases rapidly with time, but the UV extinction (FUV–U bands) increases first and then decreases with time. The reason is that the optical extinction is dominantly produced by large grains that have a short disruption time by RATD (see Hoang et al. 2019), and the production of small grains by RATD results in higher UV extinction. We also see that the amplitude of the extinction variation is smaller for more distant clouds.

3.3. Time Variation of Color Excess $E(B - V)$ and R_V

From $A(\lambda, t)$, we can calculate the color excess $E(B - V) = A_B - A_V$ and the total-to-selective extinction ratio $R_V = A_V/E(B - V)$ to understand how these quantities vary with time due to RATD.

Figure 6 (upper panel) shows the variation of $E(B - V, t)/E(B - V, 0)$ with time for the different cloud distances. For a given cloud distance, the color excess remains constant until grain disruption begins at $t \sim t_{disr}$. Subsequently, the ratio increases rapidly and then decreases to a saturated level when RATD ceases. For example, at a distance $d = 2$ pc, the color excess starts to rise at $t \sim 20$ days and declines again to the saturated value at $t \sim 40$ days.

Figure 6 (lower panel) shows the variation of R_V with time. The value R_V starts to rapidly decrease from the initial standard value of $R_V = 3.1$ to $R_V \sim 1$–1.5 after less than 40 days. The moment where R_V starts to decline is similar to that of $E(B - V)$, which is determined by the grain disruption time t_{disr} (see, e.g., Figure 1). We note that although $E(B - V)$ has some fluctuations over time, R_V tends to decrease smoothly because A_V always decreases with time, due to the disruption of large grains by RATD (see Figure 1). The time required to decrease R_V from its original value is shorter for grains closer to the source, and the terminal value of R_V is also smaller. For example, it takes only 15 days for R_V to decrease from its original value to its final value of 0.5, while at 2 pc, it takes 20 days for R_V to decrease to its final value of ∼1.4.

Figure 7 (upper panel) shows the variation of R_V with cloud distance evaluated at $t = 45$ days for various S_{max}. Dust grains with a lower S_{max} can be disrupted out to a larger distance (see Figure 2), so that R_V starts to decrease from a larger distance. On the other hand, grains with a high strength of $S_{max} \geqslant 10^9$ erg cm^{-3} can be disrupted within a small distance of $d \sim 1$ pc. Thus, one can only observe small values of R_V if the dust cloud is close to the source.

Figure 7 (lower panel) shows the variation of R_V with time for a dust cloud at a distance $d = 1$ pc. Weaker grains have R_V decreasing sooner and achieving a lower terminal value than stronger ones due to the dependence of RATD on the material strength (see Figure 2). For example, after 45 days, dust grains in a cloud at 1.5 pc will have $R_V = 1.1$ for $S_{max} = 10^7$ erg cm^{-3}, 1.4 for $S_{max} = 10^8$ erg cm^{-3}, and $R_V = 3.1$ for $S_{max} \geqslant 10^9$ erg cm^{-3}.

4. Polarization of SN Light in the Presence of RAT Alignment and RATD

4.1. Grain Alignment by RATs

Dust grains of an irregular shape can be aligned with the magnetic field by an anisotropic radiation field via the RAT mechanism (see Andersson et al. 2015 and Lazarian et al. 2015 for reviews). In the unified theory of RAT alignment, grains are first spun up to suprathermal rotation and then driven to be perfectly aligned with the ambient magnetic fields by magnetic relaxation within grains having iron inclusions (Hoang & Lazarian 2016). Therefore, grains are only efficiently aligned when they can rotate suprathermally. One can adopt a criterion for grain suprathermal rotation as follows (Hoang & Lazarian 2008):

$$\omega_{RAT}(t) \gtrsim 3\omega_T, \quad (17)$$

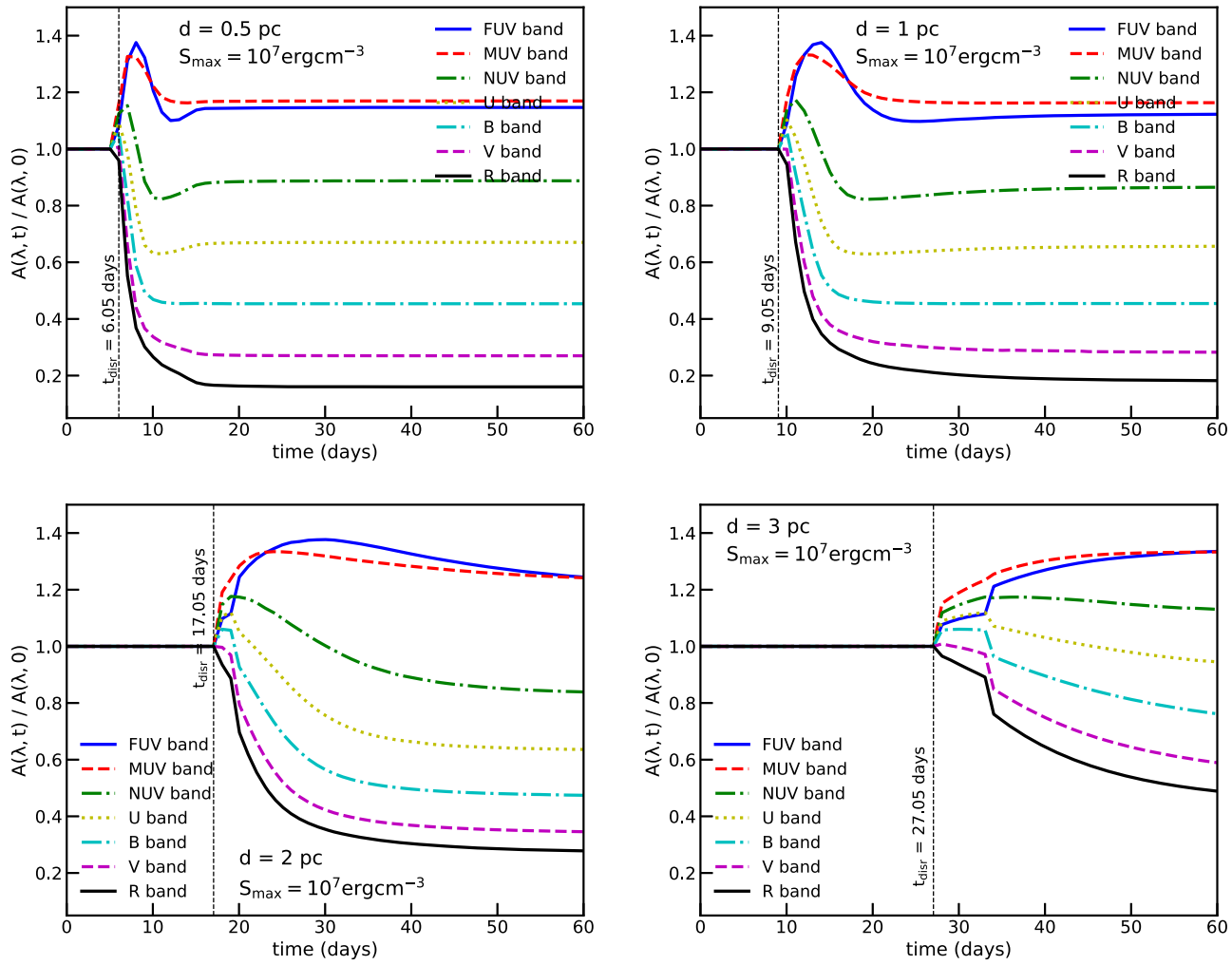

Figure 5. Variation of $A(\lambda, t)/A(\lambda, 0)$ from FUV–R bands with time for the different cloud distances. Vertical lines mark the disruption time of graphite, which occurs earlier than silicates. The ratio is constant initially and starts to vary with time when RATD begins at $t_{\rm disr}$. After the disruption ceases, the ratio is constant again.

where ω_T is the thermal angular velocity of the dust grain with kinetic energy of $kT_{\rm gas}$ given by

$$\omega_T = \sqrt{\frac{2kT_{\rm gas}}{I}} \simeq 2.3 \times 10^5 \hat{\rho}^{-1/2} T_2^{1/2} a_{-5}^{-5/2} {\rm rads}^{-1}, \quad (18)$$

where $T_2 = T_{\rm gas}/(100\ {\rm K})$.

Let $a_{\rm align}$ be the critical size of aligned grains. Then, $a_{\rm align}$ can be determined by using the suprathermal condition $\omega_{\rm RAT}(t) = 3\omega_T$.

The grain-alignment timescale is the timescale required for RATs to spin up grains to suprathermal rotation:

$$t_{\rm align} \equiv \frac{3I\omega_T}{\Gamma_{\rm RAT}} \simeq 0.6 \left(\frac{d_{\rm pc}^2}{L_8 e^{-\tau}}\right) \bar{\lambda}_{0.5}^{1.7} a_{-5}^{-2.2} T_2^{1/2} \text{ days}, \quad (19)$$

where $\Gamma_{\rm RAT}$ is given by Equation (3) with $a \lesssim \bar{\lambda}/1.8$ (see also Hoang 2017).

Figure 8 shows the variation of alignment size with time for the different cloud distances. During the first stage, the alignment size is constant, which is equal to the typical value $a_{\rm align} \sim 0.055\ \mu$m induced by the average ISRF. Due to intense SN radiation, the alignment size starts to decrease after some alignment time ($t_{\rm align}$) from the original value to smaller values. One can see that the alignment time by SNe Ia is $t_{\rm align} \sim$ 3–7 days for $d = 0.5$–3 pc. Grains in a more distant cloud have larger alignment sizes, such that small grains at 0.5 pc can be aligned up to 0.005 μm after 10 days, but it is still 0.05 μm with a cloud farther than 1 pc (see also Equation (19)).

4.2. Modeling Polarization of SNe Ia

We assume that only silicate grains can be aligned with the magnetic field, whereas graphite grains are not efficiently aligned (Chiar et al. 2006; see Hoang & Lazarian 2016 for a theoretical explanation).[5] For the magnetic field in the plane of the sky, the degree of starlight polarization per H atom due to aligned grains in units of percent is given by Hoang (2017):

$$\frac{P(\lambda)}{N_{\rm H}} = 100 \int_{a_{\rm align}}^{a_{\rm max}} \frac{1}{2} C_{\rm pol}(a) f(a) \left(\frac{1}{n_{\rm H}} \frac{dn}{da}\right) da, \quad (20)$$

where $C_{\rm pol} = Q_{\rm pol} \pi a^2$ is the polarization cross section with $Q_{\rm pol}$ the polarization efficiency, and $f(a)$ is the alignment function describing the grain-size dependence of the grain-alignment degree, and $a_{\rm max} \equiv a_{\rm disr}$. For our modeling, we

[5] Although carbonaceous grains are expected to be aligned via the k-RAT mechanism (see Lazarian & Hoang 2019), their degree of alignment is not yet quantified, in contrast to silicate grains that have their alignment degree quantified in Hoang & Lazarian (2016) using numerical simulations.

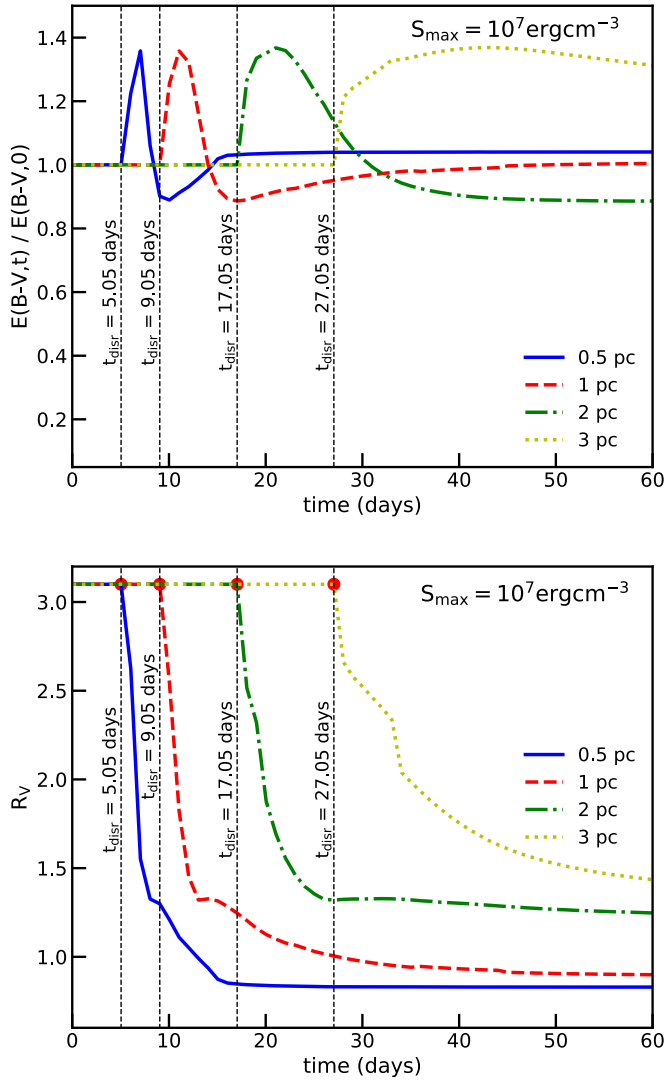

Figure 6. Time variation of $E(B-V)$ (upper panel) and R_V (lower panel) for different cloud distances and $S_{max} = 10^7$ erg cm^{-3}. Both $E(B-V)$ and R_V begin to change when grain disruption begins at $t \sim t_{disr}$ (marked by the vertical dotted lines). R_V decreases rapidly from their original values from $t = t_{disr}$ to 40 days and then almost saturates when RATD ceases.

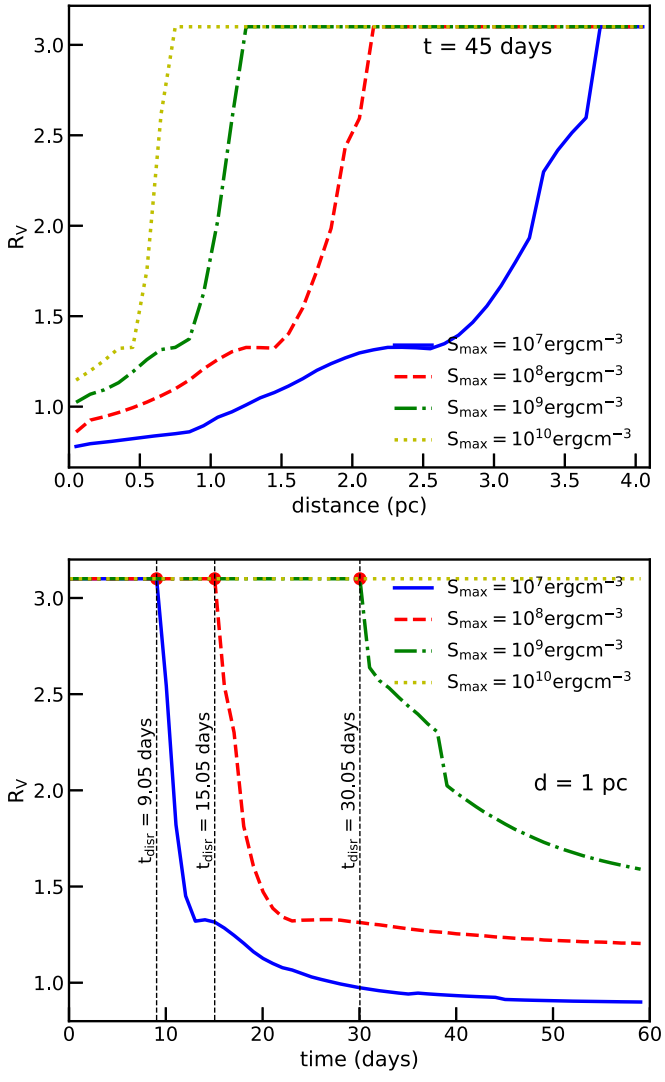

Figure 7. R_V vs. cloud distance at $t = 45$ days (upper panel), and R_V vs. time for the cloud distance of 1 pc (lower panel), assuming different values of S_{max}.

consider the oblate grain shape and take the data of Q_{pol} computed by Hoang et al. (2013).

The alignment function can be modeled by the following function:

$$f(a) = 1 - \exp\left[-\left(\frac{0.5a}{a_{align}}\right)^3\right], \quad (21)$$

which yields the perfect alignment $f(a) = 1$ for large grains of $a \gg a_{align}$ and adequately approximates the numerical results from Hoang & Lazarian (2016) as well as results from inverse modeling of starlight polarization (Hoang et al. 2014; Hoang 2017).

4.3. Polarization Curves

Figure 9 shows the polarization curve computed at different times for a dust cloud at 1 pc, assuming $S_{max} = 10^7$ erg cm^{-3} (upper panel) and $S_{max} = 10^8$ erg cm^{-3} (lower panel). At $t \lesssim$ 1 days, dust grains are aligned by the average diffuse

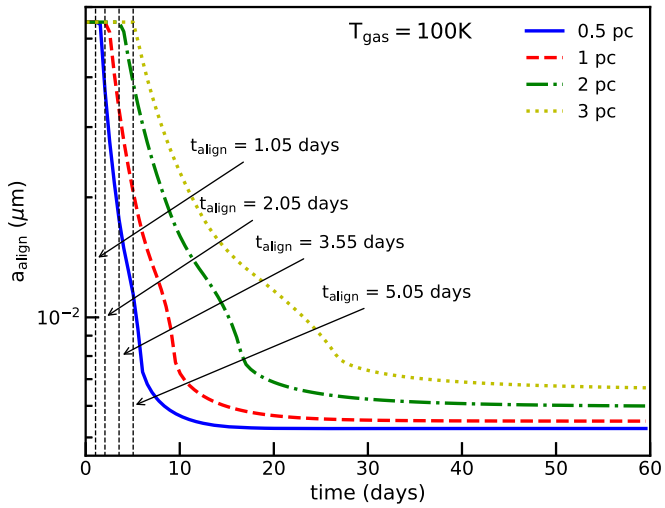

Figure 8. Critical size of grain alignment by RATs vs. time for the different cloud distances. The alignment size starts to decrease rapidly from the original value when enhanced alignment by SN radiation begins, marked by vertical dotted lines. The decrease continues to their terminal values.

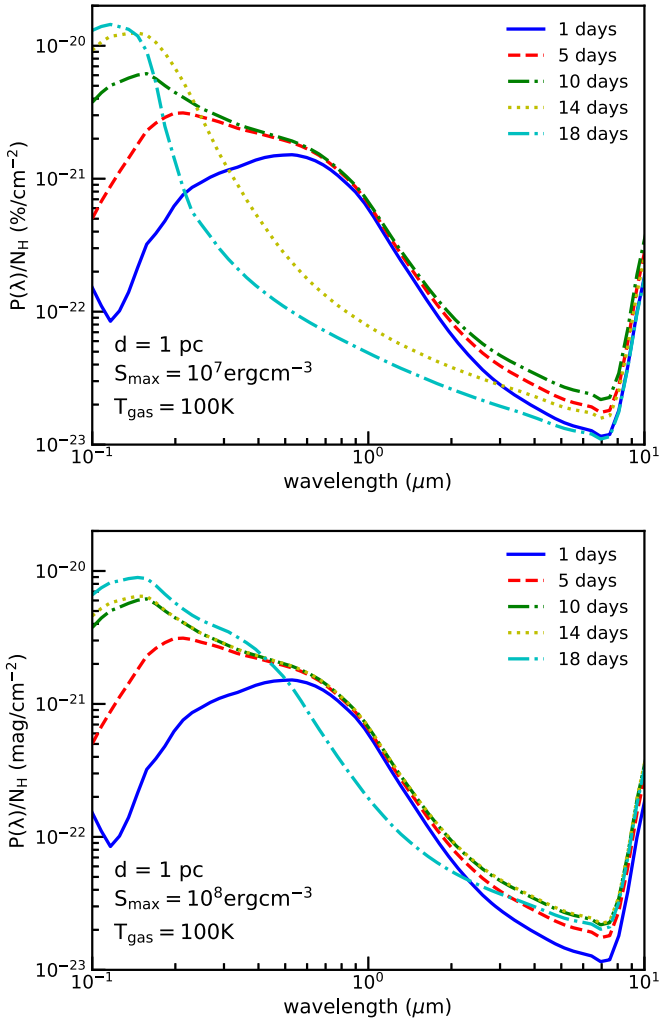

Figure 9. Polarization curves evaluated at different times for a dust cloud at 1 pc, assuming $S_{max} = 10^7$ erg cm^{-3} (upper panel) and $S_{max} = 10^8$ erg cm^{-3} (lower panel). Enhanced alignment of small grains induces the blueshift of the peak wavelength. The RATD effect reduces polarization at $\lambda > 0.3$ μm, and the efficiency is weaker for higher S_{max}.

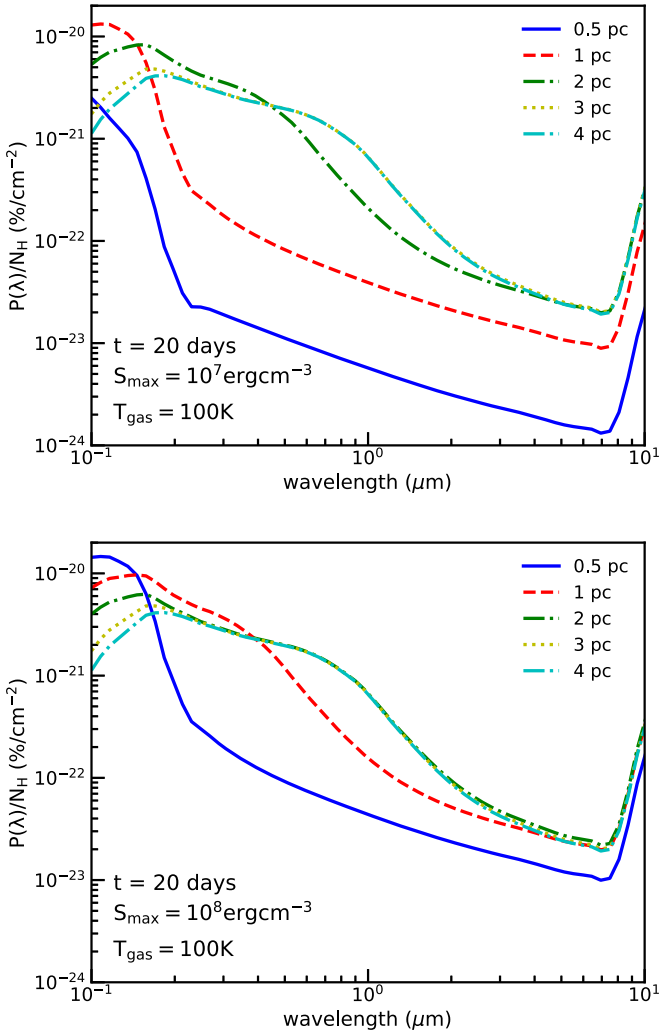

Figure 10. Polarization curves evaluated at $t = 20$ days for different cloud distances, assuming $S_{max} = 10^7$ erg cm^{-3} (upper panel) and $S_{max} = 10^8$ erg cm^{-3} (lower panel).

interstellar radiation, so the maximum polarization occurs at $\lambda_{max} \sim 0.55$ μm. After that, SN radiation dominates and makes smaller grains aligned. As a result, the UV polarization is increased rapidly, and the peak wavelength λ_{max} is decreased. The degree of optical–NIR polarization ($\lambda > 0.5$ μm) is slightly increased. After $t \sim 10$ days, grain disruption by RATD begins (see Figure 1), reducing the abundance of large grains. Therefore, the degree of optical–NIR polarization decreases substantially, which results in a narrower polarization profile compared to the original polarization curve.

Figure 9 (lower panel) shows similar results, but for $S_{max} = 10^8$ erg cm^{-3}. The same trend as the upper panel is observed, but the significant decrease of optical–NIR polarization is only seen at a later time of $t \gtrsim 14$ days because grains of stronger material require more time to disrupt (see Figure 2). One will note that the polarization curves at 10 days and 14 days are very similar, revealing that grain alignment is saturated.

Figure 10 shows the polarization curves calculated at $t = 20$ days for the different cloud distances, assuming $S_{max} = 10^7$ erg cm^{-3} (upper panel) and $S_{max} = 10^8$ erg cm^{-3} (lower panel). The optical–NIR polarization decreases significantly with decreasing cloud distance because grains closer to the source experience stronger rotational disruption (see Figure 2). At the same time, the peak wavelength λ_{max} is smaller for grains at smaller distances, due to the more efficient alignment of grains by RATs.

Above, we have assumed that only silicate grains are aligned with the magnetic field. Nevertheless, the peak wavelength of polarization would be not much different when carbonaceous grains are assumed to be aligned, because it mostly depends on the alignment function.

4.4. Time Variation of Dust Polarization and Peak Wavelength

Figure 11 shows the temporal variation of $P(\lambda, t)/P(\lambda,0)$ from the FUV to R bands for the different cloud distances. During the initial stage, the ratio $P(\lambda, t)/P(\lambda,0)$ is constant; however, this stage is rather short, between 1 and 5 days, corresponding to the alignment timescale t_{align} (see Figure 8; also Hoang 2017). After that, the polarization degree increases gradually, and this rising period continues until $t \sim 5$–30 days until grain disruption by RATD begins (i.e., at $t = t_{disr}$) for $d = 0.5$–3 pc. After that, the polarization degree then declines

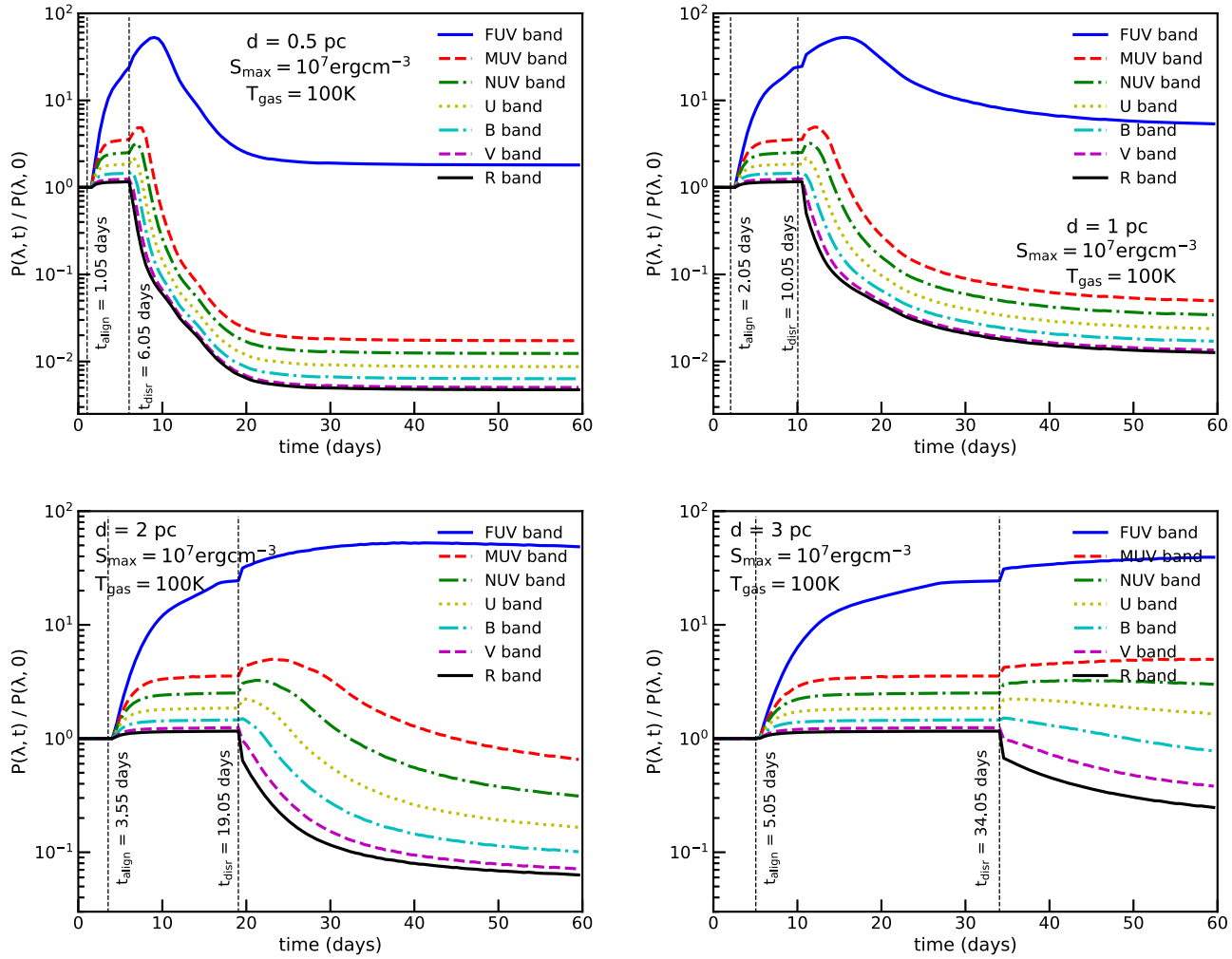

Figure 11. Ratio $P(\lambda, t)/P(\lambda, 0)$ vs. time from the FUV to V bands for different cloud distances assuming $S_{\rm max} = 10^7$ erg cm^{-3}. Optical/NIR polarization degree first increases due to enhanced alignment by RATs and then decreases when grain disruption by RATD starts. Dotted vertical lines mark the alignment time ($t_{\rm align}$) and disruption time ($t_{\rm disr}$) of silicate grains.

rapidly and achieves a saturated level when RATD ceases, which occurs after $t \sim 20$ days for $d = 0.5$ pc and 40 days for $d = 1$ pc, respectively. In summary, due to RAT alignment and RATD, the polarization degree increases from $t_{\rm align}$ to $t_{\rm disr}$, and it decreases rapidly at $t > t_{\rm disr}$.

Figure 12 (upper panel) presents the variation of the peak wavelength with time for dust clouds at different locations and $S_{\rm max} = 10^7$ erg cm^{-3}. Initially, $\lambda_{\rm max} \sim 0.55\ \mu$m is produced by grains aligned by the ISRF (Hoang & Lazarian 2014). In the presence of strong SN radiation, smaller grains can be aligned, resulting in a rapid decrease of $\lambda_{\rm max}$. Dust grains at farther distances receive lower radiation energy density such that $\lambda_{\rm max}$ starts to decrease later and stops at higher $\lambda_{\rm max}$. For example, dust at 0.5 pc gives $\lambda_{\rm max} \leqslant 0.5\ \mu$m after $\sim$1 day and stops at 0.1 μm, while dust at 3 pc needs $\sim$8 days to begin and gives the minimum $\lambda_{\rm max} \sim 0.15\ \mu$m.

Figure 12 (lower panel) shows the comparison of $\lambda_{\rm max}$ over 60 days with (solid line) and without (dashed line) dust disruption. As shown, the values of $\lambda_{\rm max}$ in the two cases are similar in the early times and become different when grain disruption begins. Their difference is larger at a shorter distance because grain disruption is stronger.

The dashed line shows that alignment grain size saturates earlier than disruption grain size, such that $\lambda_{\rm max}$ remains unchanged just after 10 days (for grains at 0.5 pc) and 20 days (for grains at 2 pc). The slower disruption rate for the distant cloud will make $\lambda_{\rm max}$ constant over a longer period.

4.5. Effect of the Size-dependent Tensile Strength

Until now, we have been calculating the grain disruption size, $R_{\rm V}$, and $\lambda_{\rm max}$ by assuming that the maximum tensile strength is constant for all grain sizes. A more realistic situation is that small grains would have compact structures and thus have a higher $S_{\rm max}$. To see how the size-dependent tensile strength affects our results, we now assume $S_{\rm max} = 10^7$ erg cm^{-3} for grains larger than $\sim$0.05 μm and $S_{\rm max} = 10^9$ erg cm^{-3} for grains smaller than 0.05 μm.

Figure 13 (top panel) shows the grain disruption size for a constant $S_{\rm max}$ (dashed lines) and the $S_{\rm max}$ varying with grain size (solid lines) for different cloud distances. In the latter case, the grain disruption size decreases to a final value of 0.05 μm if the radiation energy density is not strong enough to destroy further.

The same as the top panel, but the middle panel shows $R_{\rm V}$ versus time for a fixed (dashed lines) and changing $S_{\rm max}$ (solid lines). The $R_{\rm V}$ values in the two cases decrease rapidly with time, but the latter case has higher terminal values of $R_{\rm V} \sim 1.45$, due to the larger disruption sizes (see top panel).

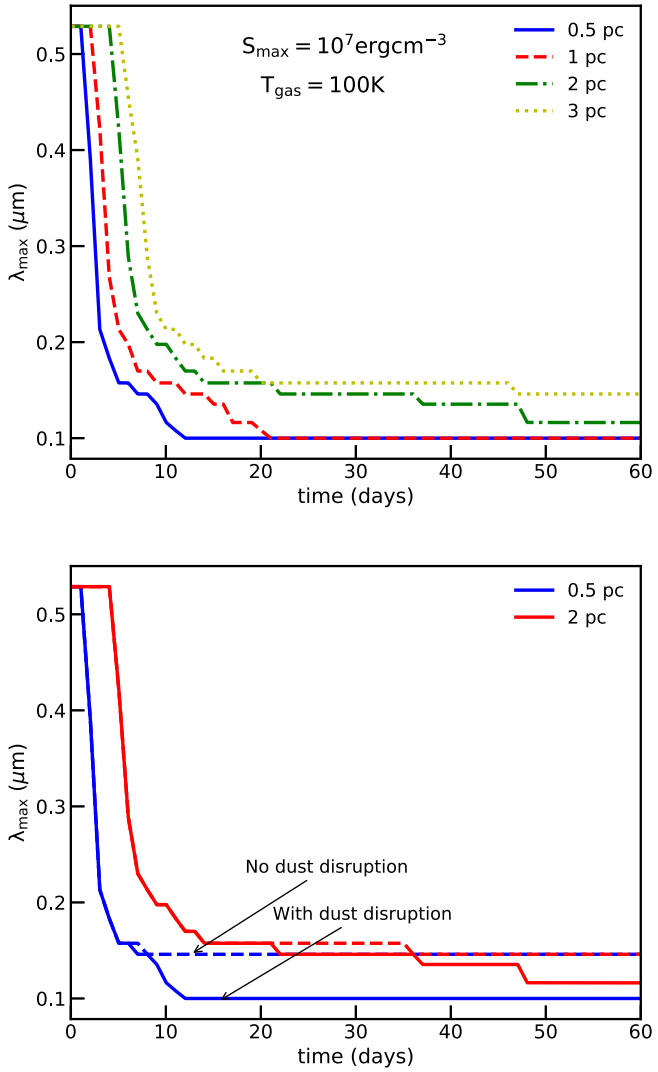

Figure 12. Upper panel: decrease of the peak wavelength λ_{max} with time over 60 days under the effect of RAT alignment and disruption, assuming a dust cloud between 0.5 and 3 pc and $S_{max} = 10^7$ erg cm^{-3}. Lower panel: comparison of λ_{max} with time for cloud distances of 0.5 and 2 pc with RATD (solid line) and without RATD (dashed line). RATD has a smaller effect on the peak wavelength than the alignment by RATs.

Figure 13 (bottom panel) shows the time dependence of λ_{max} over 60 days for constant (dashed lines) and changing S_{max} (solid lines). For the latter case, the terminal peak wavelength is slightly larger than the former case, i.e., $\lambda_{max} = 0.13\,\mu$m at 1 pc and $\lambda_{max} = 0.15\,\mu$m at 2 pc. From the middle and top panels, it appears that the effect of changing S_{max} has a more important effect on R_V than on λ_{max}.

5. Effect of RATD on the SN Ia Lightcurve

In Section 3, we have shown that the disruption of large grains into smaller ones by RATD can increase the dust extinction in the NUV band and decrease the extinction in the optical and NIR bands over time. As a result, the observed radiation spectrum of SNe Ia would be different from the case where dust properties are constant, i.e., in the absence of RATD. In this section, we use the new extinction curve calculated from Section 3 to predict how the SN Ia lightcurve changes with time in the presence of RATD.

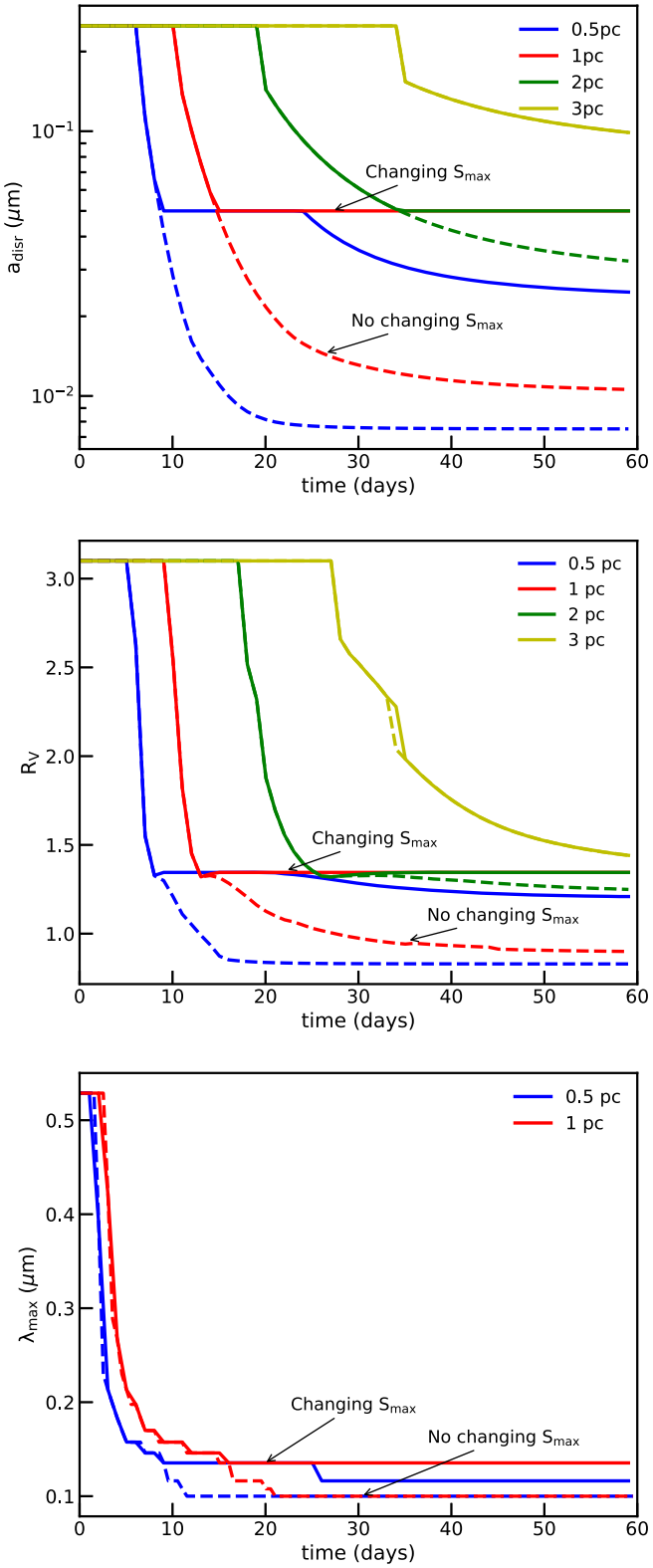

Figure 13. Comparison of a_{disr} (top panel), R_V (middle panel), and λ_{max} (bottom panel) vs. time with constant (dashed lines) and changing S_{max} (solid lines).

Let us first derive a simple intrinsic lightcurve of SNe Ia. The explosion of SNe Ia releases a vast amount of energy and ejects all material into the surrounding space in a short time. The radius of such an expanding fireball will increase dramatically, and the temperature will drop during the free expansion phase. For our

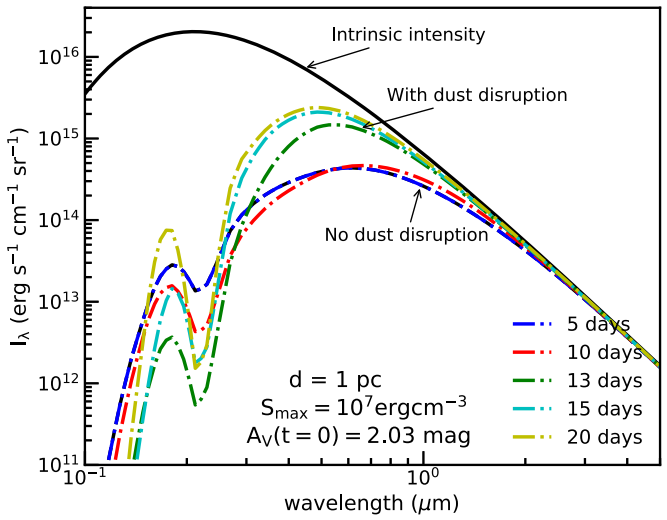

Figure 14. Comparison of the intrinsic radiation intensity from an SN Ia (black line) with the radiation intensity attenuated by dust extinction evaluated at the different times from 5 to 20 days (dashed lines), assuming the cloud distance of $d = 1$ pc.

simple model, we assume a constant total kinetic energy $E \sim 10^{51}$ erg during this phase, and the ejecta of mass $M_{ej} = 1.4\,M_\odot$ will move with a constant velocity of $v = \sqrt{2E/M_{ej}} \sim 10^4 E_{51}^{1/2} (M_\odot/M_{ej})^{1/2}$ km s^{-1} with $E_{51} = E/10^{51}$ erg. The total bolometric luminosity of SNe Ia can be estimated by

$$L_{bol} = 4\pi R^2 \sigma T_{SN}^4, \quad (22)$$

where $R = vt$ is the radius of SNe Ia after time t, and T_{SN} is its effective temperature. Using L_{bol} from Equation (1), the effective temperature of SNe Ia decreases with time as

$$T_{SN} \simeq 10^4 \left(\frac{L_{bol}}{10^9\,L_\odot}\right)^{1/4} \left(\frac{10^4 \text{ km s}^{-1}}{v}\right)^{1/2} \left(\frac{t}{1 \text{ days}}\right)^{1/2} \text{K}. \quad (23)$$

The intensity of SN radiation after propagating through a dusty cloud at wavelength λ is governed by

$$I_\lambda(t) = I_\lambda^0 e^{-\tau(\lambda,t)}, \quad (24)$$

where

$$I_\lambda^0 = \frac{2hc^2}{\lambda^5} \frac{1}{\exp(hc/\lambda k T_{SN}) - 1} \quad (25)$$

is the intrinsic specific radiation intensity and the optical depth $\tau(\lambda, t) = A(\lambda, t)/1.086$. Here, infrared thermal emission from dust grains is disregarded because we are interested only in the UV–NIR spectrum of SNe Ia. With the $A(\lambda, t)$ obtained in Section 3, one can calculate the observed radiation intensity via Equation (24).[6]

Figure 14 shows the UV–NIR spectrum of an SN Ia observed at different times (dashed and dotted–dashed lines) compared with the intrinsic spectrum (solid black line). We assume an original visual extinction estimated for SN 1986G of $A_V = 2.03$ mag to derive the total gas column density $N_H = 3.14 \times 10^{21}$ cm^{-2}. The black dashed line represents the observed SN spectrum with a constant dust extinction of $A_V(t = 0) = 2.03$ (no disruption), and the color dotted–dashed line shows the results when RATD is taken into account. Without RATD, the observed SN spectrum appears constant with time but will vary in the presence of RATD. Indeed, due to RATD, large grains are disrupted in smaller grains, increasing the extinction at the NUV band, such that SNe Ia become redder. In contrast, the decrease of the extinction in the optical and NIR bands due to grain disruption causes SNe Ia to rebrighten over time. The radiation intensity at long wavelengths ($\lambda \sim 3$–$5\,\mu$m) is not affected by dust disruption because of an optically thin regime (see Section 3).

To see more details about the time variation of SN colors, in Figure 15 we show the specific intensity at FUV (0.15 μm), MUV (0.25 μm), NUV (0.3 μm), and U, B, V, and R bands for the different dust cloud locations, assuming $S_{max} = 10^7$ erg cm^{-3}. In the absence of RATD, the radiation intensity of SNe Ia at the different bands only decreases with time due to the decrease of T_{SN}. However, in the presence of RATD, the radiation intensity from optical–NIR wavelengths exhibits an abrupt increase (i.e., SNe rebrighten), whereas it has a drop at FUV–NUV bands (solid lines), due to the effect of grain disruption. The "rebrightening" time in optical–NIR is longer for more distant clouds. For instance, the rebrightening time $t_{rebright} \sim t_{disr} \sim 10$ days for $d = 0.5$ pc and $t_{rebright} \sim 30$ days for $d = 3$ pc.

Figure 16 presents the same results as Figure 15 but with grains with $S_{max} = 10^8$ erg cm^{-3}. One can see that the large disruption grain size of stronger grains has a smaller effect on the dust extinction in the UV–NIR band than the weak grains. As a result, the "rebrightening" and "redimming" features due to the reduction of the visible extinction and increase in extinction at the FUV–NUV band become smaller, and there is nearly no effect if the cloud is farther than 2 pc.

Note that to get insights into the effect of RATD on the observed SN Ia lightcurve, we have modeled the intrinsic SNe Ia lightcurve as a fireball with a constant expansion velocity. However, the radioactivity of synthesized Ni^{56} and Co^{56} (Arnett 1982) can provide more radiative energy, such that the peak luminosity of SNe Ia and the effective temperature would be different from our simplified model. Nevertheless, we expect that the effect of RATD on the SN lightcurve is similar.

6. Discussion

6.1. Comparison of R_V and λ_{max} from Our Models with SN Ia Data

Using RATD theory, we have computed the extinction curves $A(\lambda, t)$ by dust grains, which have their size distribution being modified by RATD at the different times and dust cloud distances given in Section 3.3. Our obtained results show that, due to RATD, R_V rapidly decreases with time, from an original value of $R_V = 3.1$ to small values of $R_V \sim 1.5$ after a timescale $t_{disr} \sim 50$–60 days if the dust cloud is located within $d \sim 4$ pc from the SN (see Figure 6). The final R_V value achieved when RATD ceases is smaller for the dust cloud closer to the SN, but it increases with the tensile strength of grains (see Figures 6). Comparing our results with the observational data of SNe Ia (see Table 1), one can see that RATD can successfully reproduce the unusually low values of R_V observed toward many SNe Ia (see Table 1; Burns et al. 2014; Cikota et al. 2016).

[6] Here, to illustrate the effect of time-varying dust extinction, we disregard the rising phase of the SN lightcurve. With the $A(\lambda, t)$ available from Section 3, one can predict the observed intensity for an accurate intrinsic intensity without difficulty.

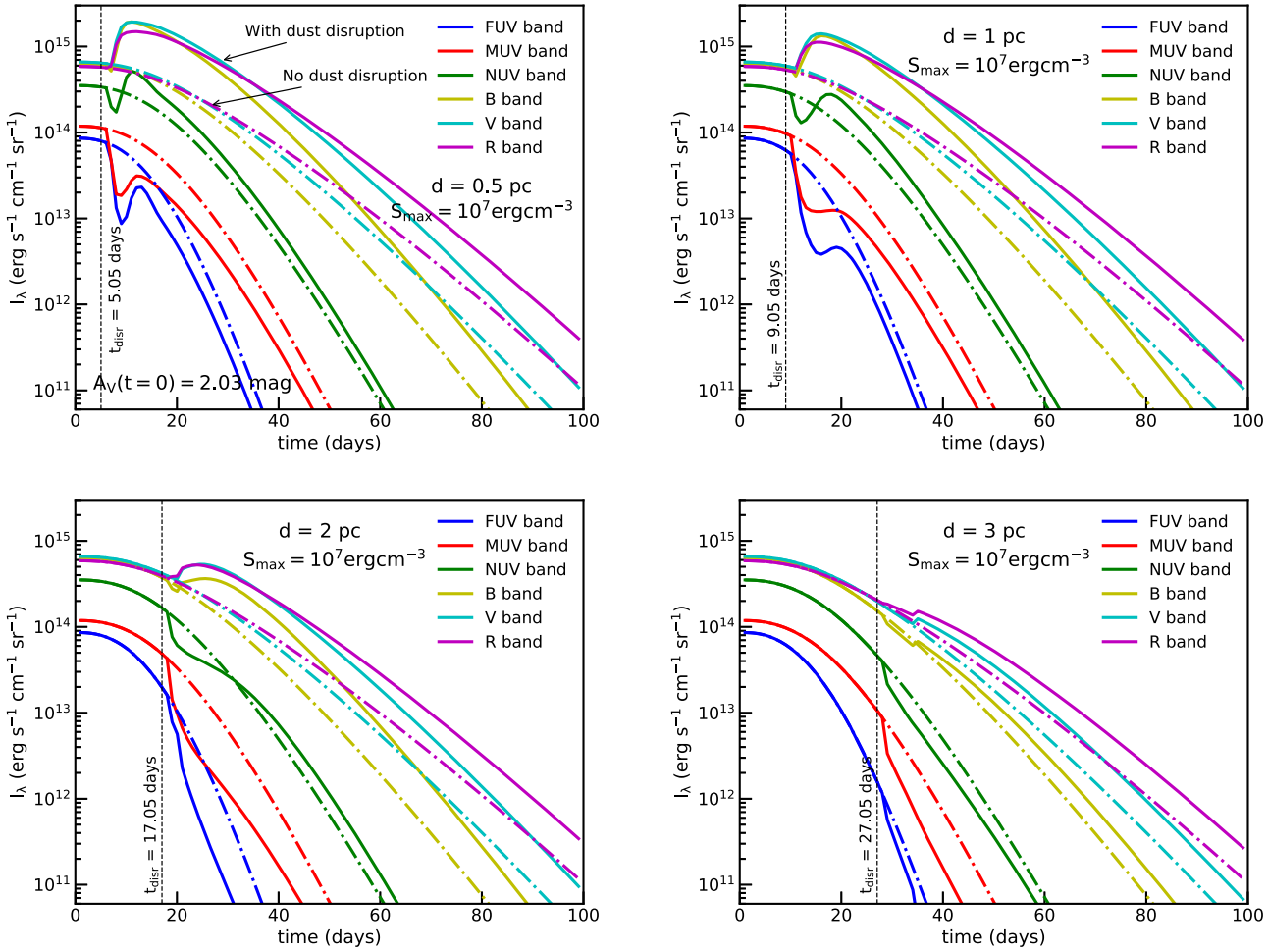

Figure 15. Specific intensity at the different bands as a function of time without (dashed lines) and with (solid lines) rotational disruption, assuming the different dust cloud distances from 0.5 to 3 pc. The tensile strength $S_{max} = 10^7$ erg cm^{-3} is considered. Vertical dotted lines mark the disruption time of graphite grains.

Table 1
Physical Parameters of SNe Ia (Phillips et al. 2013; Amanullah et al. 2014; Hoang 2017)

SNe	$\lambda_{max}(\mu m)$	K	R_V	A_V(mag)	$E(B-V)$(mag)
1986G	0.43	1.15	2.57	2.03	0.79
2006X	0.36	1.47	1.31	1.88	1.44
2008fp(mod1)	0.15	0.40	1.20	0.71	0.59
2008fp(mod2)	0.41	1.03	2.20	0.29	0.13
2014J(mod1)	0.05	0.40	1.40	1.85	1.37
2014J(mod2)	0.35	1.15	2.59	1.17	0.45
SN 2007le	0.3967 ± 0.0494	1.73 ± 0.87	1.46 ± 0.28	0.54 ± 0.08	0.39
SN 2010ev	0.4408 ± 0.0114	1.89 ± 0.23	1.54 ± 0.58	0.50 ± 0.18	0.32
SN 2007fb	0.3821 ± 0.0447	1.13 ± 0.46	2.17 ± 0.57	$\leqslant$0.09	$\leqslant$0.03
SN 2003W	0.3996 ± 0.0371	2.56 ± 1.03	1.00 ± 0.70	0.30	0.29
SN 2007af	0.7409 ± 0.0537	1.24 ± 0.35	2.11 ± 0.51	0.31	0.15
SN 2002fk	0.4403 ± 0.0460	0.57 ± 0.35	1.73 ± 1.02	0.03	0.02
SN 2002bo	0.3525 ± 0.0137	3.95 ± 0.49	1.22 ± 0.26	0.62 ± 0.10	0.53
SN 2011ae	0.4256 ± 0.0295	3.56 ± 1.87	...	...	...
SN 2005hk	0.6731 ± 0.2116	−1.36 ± 1.51	3.1	0.22 ± 0.06	0.07

Note. SN 1986G: Hough et al. (1987); SN 2006X: Patat et al. (2009); SN 2008fp and SN 2014J: Cox & Patat (2014), Patat et al. (2015), Kawabata et al. (2014), and Hoang (2017). Data for the last SN Ia, SN 2005hk, are taken from Zelaya et al. (2017).

We also modeled the polarization of SN Ia light by grains aligned with the magnetic fields using the RAT mechanism in Section 4. Our results show that the peak wavelength λ_{max} decreases from the standard ISM value of $\sim$0.55 μm to $\lambda_{max} < 0.2\,\mu$m due to RAT alignment after a timescale of $t_{align} \sim$ 5–20 days for clouds within a distance of 4 pc (see

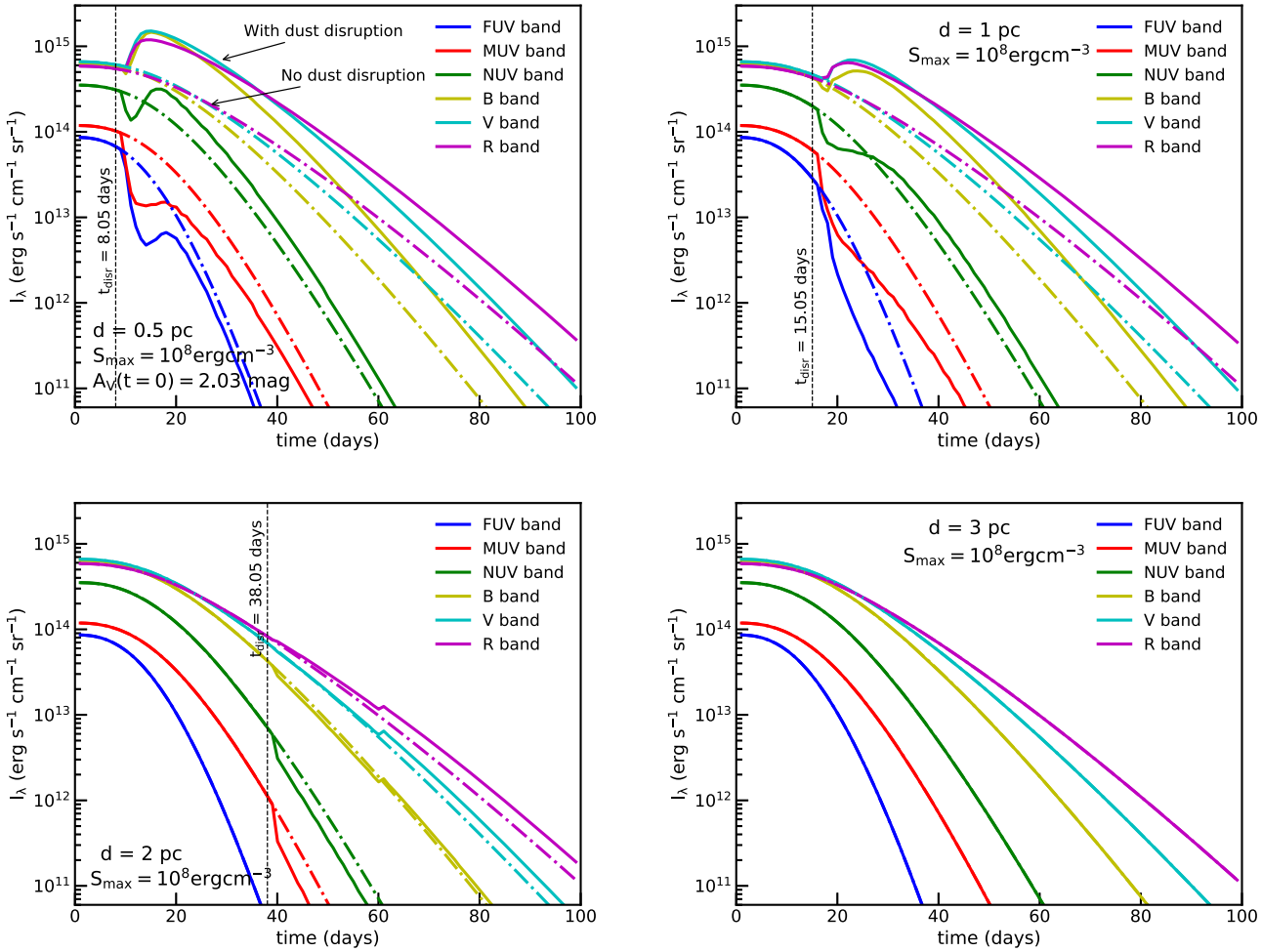

Figure 16. Same as Figure 15 but for grains with $S_{max} = 10^8$ erg cm^{-3}.

Figure 12, upper panel). These results can reproduce the low values of λ_{max} observed toward SNe Ia (see Table 1; Patat et al. 2015; Zelaya et al. 2017). We note that the characteristic timescale for achieving the terminal value of λ_{max} is much shorter than that for the terminal value of R_V because $t_{align} < t_{disr}$.

From the lower panel of Figure 12, one can see that the main reason for the decrease of λ_{max} from 0.5 to 0.2 μm is due to the alignment of small grains by the RAT mechanism, as suggested by Hoang (2017). Therefore, to obtain a higher λ_{max}, one can increase the critical limit for suprathermal rotation, i.e., T_{gas}.

Figure 17 shows the peak wavelength of the dust polarization toward SNe Ia for the different gas temperatures and the dust cloud at 3 pc from the source. Here, the grain disruption is not considered in order to focus on the effect of grain alignment. The peak wavelength increases with increasing T_{gas} because a higher temperature results in a larger ω_T such that stronger radiation energy is required to spin up grains to suprathermal rotation and align grains efficiently. For example, a dust cloud at 3 pc will give $\lambda_{max} \sim 0.3\,\mu$m if $T_{gas} = 100{,}000$ K, higher than two times $\lambda_{max} = 0.15\,\mu$m if $T_{gas} = 1000$ K after 60 days.

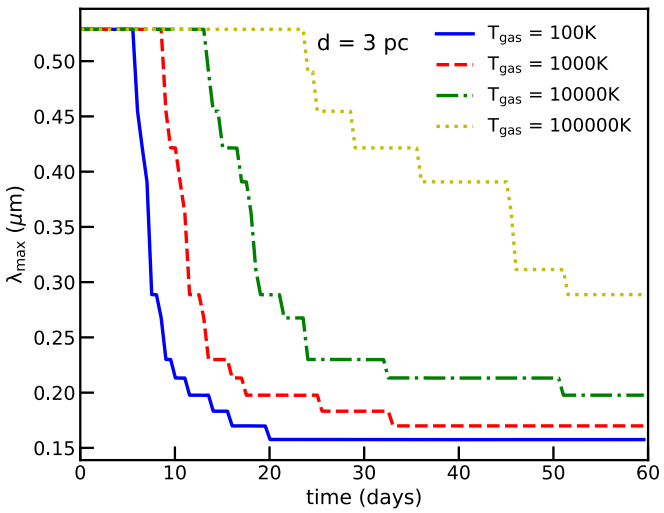

Figure 17. The peak wavelength λ_{max} over 60 days for different gas temperatures and cloud distance $d = 3$ pc, assuming no dust disruption.

6.2. Test RATD and RAT Alignment Mechanisms with Time Variation of SN Ia Extinction and Polarization

Our theoretical models of dust extinction toward SNe Ia in the presence of RATD reveal that the extinction and R_V remain constant until the grain disruption occurs at $t = t_{disr}$, which spans from 5 to 30 days, depending on the cloud distance (right panel of Figure 6) and grain tensile strength S_{max} (Figure 7). Beyond t_{disr}, the optical–NIR extinction and R_V decrease rapidly and achieve saturated levels after 50–60 days for cloud distances $d < 4$ pc. Therefore, by observing SNe Ia at early

times and inferring the time variation of R_V, one can test the RATD mechanism.

On the other hand, our theoretical models of dust polarization due to grains aligned by the RAT mechanism show that the dust polarization starts to increase after a timescale corresponding to the alignment timescale, $t_{\rm align}$, which spans between 3 and 10 days (see Figures 9 and 10). When grain disruption by RATD begins at $t \sim t_{\rm disr} > t_{\rm align}$, the polarization starts to decrease rapidly over time, and its time variation is similar to that of the extinction. Therefore, the best strategy for testing the RAT alignment mechanism is to observe the SN Ia polarization at the earliest times, $t <$ 5–15 days, if the dust cloud is located within 4 pc from the source.

6.3. Effect of RATD on the Colors and Lightcurves of SNe Ia

Dust extinction is considered the most critical systematic uncertainty for SNe Ia cosmology (Scolnic et al. 2019). Understanding better the intrinsic lightcurves will allow for a better study of the physical properties and evolution of SNe Ia (Burns et al. 2014) and a precise measurement of the cosmological constant and a better constraint on dark energy.

Usually, to infer the intrinsic colors of SNe Ia, one adopts a typical dust model and their extinction curve and fit to the observational data. However, the dust properties around SNe Ia are shown to be modified by SN radiation, and their extinction curves are fundamentally different from the standard dust model if there exist some dust clouds within 4 pc from the source. In this situation, the intrinsic lightcurve has high accuracy when one uses observational data obtained during the first 10 days after the explosion during which the grain disruption has not yet occurred.

The situation becomes more complicated due to the time variation of the intrinsic colors of SNe Ia (Goobar 2008) and the color excess $E(B-V)$ under the effect of RATD (see Figure 6, upper panel). We predict that $E(B-V)$ first slightly increases with time after the disruption happens then decreases slowly after. Interestingly, this trend is observed toward many SNe Ia, e.g., SN 2007cs and SN 2006br, which cannot be explained by the model proposed by Bulla et al. (2018a) as for the other cases of SNe Ia. Besides, their estimated dust locations are about 1 pc from SNe, and it takes ∼10 days to observe the increase of $E(B-V)$, which nearly matches with our predictions at this cloud distance (see Figure 3 in Bulla et al. 2018b). Therefore, the modified dust model by RATD may be a reasonable explanation for the weird trend of $E(B-V)$ reported in SN 2007cs and SN 2006br.

6.4. Constraining the Distance and Properties of Dusty Clouds toward SNe Ia with Observations

Understanding the physical properties of dust clouds and their distances to SNe Ia is essential for inferring the intrinsic SN lightcurve as shown previously (Goobar 2008; Bulla et al. 2018a) as well as in this paper.

In Section 5, our theoretical modeling predicts that SNe Ia will rebrighten at optical–NIR bands accompanied by a sudden dimming at UV bands when grain disruption begins. The rebrightening time is essentially the same as the disruption time $t_{\rm disr}$, which is a function of the cloud distance to the source (Hoang et al. 2019). Therefore, one can constrain the cloud distance by observing the SN Ia colors and identify the rebrightening time. On the other hand, the polarization at optical–NIR bands decreases substantially due to RATD. As a result, a simultaneous decrease in the polarization and the rebrightening of SNe Ia would be smoking-gun evidence of the RATD mechanism.

We note that the distance of dust clouds to SNe Ia was constrained in Bulla et al. (2018b) using the time variation of the color excess $E(B-V)$ caused by scattering of photons by dust. However, their analysis still assumed a standard grain-size distribution from the Milky Way that cannot reproduce the unusually low values of R_V and $\lambda_{\rm max}$.

The physical and chemical properties of dusty clouds near SNe Ia are also poorly known. Usually, one derives the gas column density of the dust cloud using the standard relationship $N_{\rm H}/A_V \approx 5.8 \times 10^{21}\,{\rm cm^{-2}\,mag^{-1}}/R_V$ (Draine 2003). Yet, the optical extinction decreases with time from the original value if the cloud is located within 4 pc from the source (see Figure 3). Therefore, the estimate of $N_{\rm H}$ using the observed A_V would yield a lower value than the actual column density.

6.5. On the Origin of the Anomalous $K-\lambda_{\rm max}$ and $\rm K{-}R_V$ Relationships of SNe Ia

The polarization curve of distant stars in the Milky Way is usually fitted by the Serkowski law (Serkowski et al. 1975):

$$P_{\rm Serk}(\lambda) = P_{\rm max}\exp\left[-K\ln^2\left(\frac{\lambda_{\rm max}}{\lambda}\right)\right], \quad (26)$$

where $P_{\rm max}$ is the maximum degree of polarization, $\lambda_{\rm max}$ is the peak wavelength, and K is a parameter given by Wilking et al. (1980) and Whittet et al. (1992):

$$K = 0.01 \pm 0.05 + (1.66 \pm 0.09)\,\lambda_{\rm max}. \quad (27)$$

Nevertheless, Patat et al. (2015) and Cikota et al. (2018) showed that the observational data of SNe Ia (see Table 2 in Appendix B) do not follow the standard relationship (Equation (27)). Specifically, the K value for a given small $\lambda_{\rm max}$ is much larger than predicted by Equation (27). This puzzle once again reveals the abnormal properties of dust in the local environments of SNe Ia.

Our theoretical results in Section 4 reveal that the polarization curve tends to become narrower, i.e., the parameter K tends to increase, whereas the value of $\lambda_{\rm max}$ decreases in the presence of RATD (see Figures 9, 10, and 12). To see whether the RATD mechanism can reproduce such an observed anomalous relationship of K–$\lambda_{\rm max}$, we fit the Serkowski law (Equation (26)) to the polarization curve calculated using Equation (20) to obtain K and $\lambda_{\rm max}$ (see Appendix C for more details) and compare with the observational data.

Figure 18 (upper panel) shows the peak wavelength $\lambda_{\rm max}$ and the parameter K for several values of the grain disruption size from $a_{\rm disr} = 0.2$ to $0.05\,\mu$m. For each value $a_{\rm disr}$, the alignment size is varied from $a_{\rm align} = 0.05$ to $0.002\,\mu$m to account for the effect of enhanced alignment by SN light (see Appendix C for more details). Observational data from SNe Ia and some stars in our galaxy (see Tables 1 and 2) are shown for comparison. We see that, for a given $a_{\rm disr}$, K decreases rapidly with decreasing $\lambda_{\rm max}$ due to the decrease of $a_{\rm align}$. Moreover, for a given $a_{\rm align}$, $\lambda_{\rm max}$ tends to decrease with decreasing $a_{\rm disr}$. In particular, we can see that the high K values of SNe Ia can be reproduced by our models with RATD at different $a_{\rm disr}$. For example, the data of SN 2010ev (with $\lambda_{\rm max} = 0.4408 \pm 0.0114\,\mu$m) can be explained by our model with $a_{\rm disr} = 0.2\,\mu$m and $a_{\rm align} \approx 0.04\,\mu$m. Similarly, the

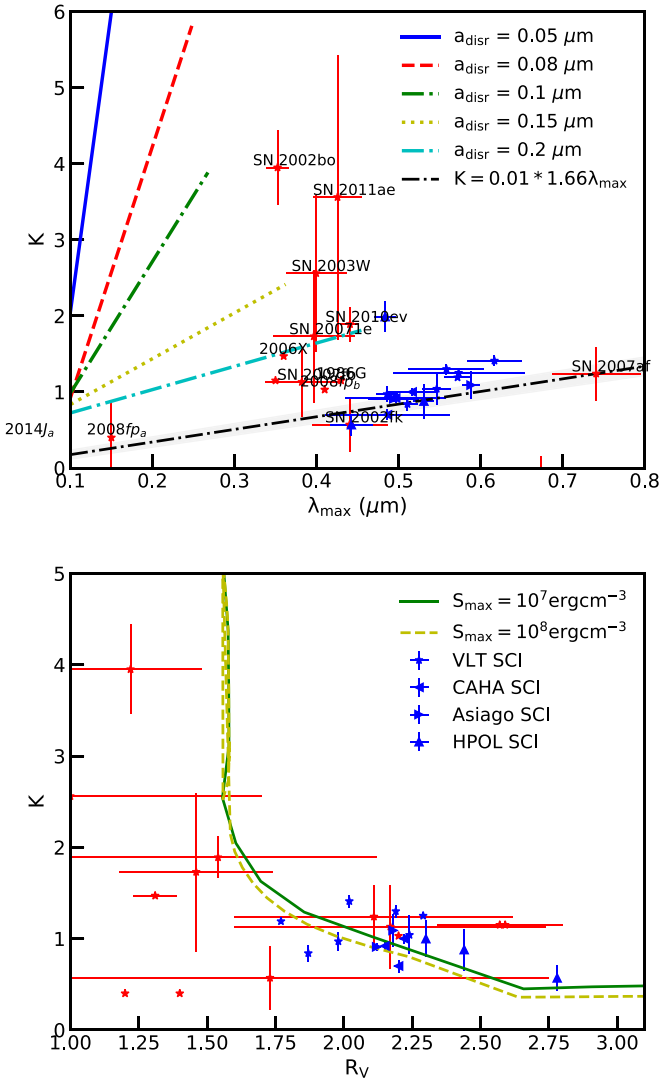

Figure 18. Upper panel: relationship between K and λ_{max} predicted by our model for different disruption sizes and alignment sizes. The black line is the standard relationship given by Equation (27). Lower panel: K vs. R_V from our models compared with observational data for SNe Ia. Symbols show observational data for SNe Ia presented (red symbols) and normal stars in our galaxy (blue symbols) listed in Tables 1 and 2.

data of SN 2006X with $\lambda_{max} = 0.36\,\mu$m can be explained by our model with $a_{disr} \sim 0.2\,\mu$m and $a_{align} \sim 0.03\,\mu$m.

We note that the polarization data of SNe Ia shown in Table 1 are measured using ground-based telescopes, which exhibit strong scatter at $\lambda \lesssim 0.4\,\mu$m due to atmospheric effects (Patat et al. 2015). Thus, the maximum polarization wavelength of $\lambda_{max} \sim 0.05$–$0.4\,\mu$m of SNe Ia is not accurately constrained (see Table 1). Moreover, Rayleigh scattering by CS matter can also induce UV polarization (Andersson et al. 2013), which would affect the model parameters (λ_{max}, P_{max}, and K) inferred from fitting the Serkowski law to the observed polarization (Hoang 2017). However, whether there exists CS matter around these SNe Ia or/and what the exact amount is are unclear.

Lastly, our results in Sections 3 and 4 show that under strong radiation fields, both extinction and polarization curves are modified from the standard curve in the ISM, which suggests some potential correlation between R_V and K. Indeed, Figure 18 (lower panel) shows the values of R_V and K calculated over 100 days for the cloud at 1 pc for several maximum tensile strengths. Observation data of SNe Ia (see Tables 1 and 2) are also shown for comparison. The predicted increase of K with decreasing R_V as a result of RAT alignment and RATD appears to be consistent with the observational data.

7. Conclusions

In this paper, we have studied the effects of rotational disruption and the alignment of dust grains by radiative torques on the extinction, polarization, and lightcurves of SNe Ia. The main findings of our study are summarized as follows:

1. Based on the RATD mechanism, grains can be disrupted when radiative torques spin them up to a critical angular velocity beyond which the induced centrifugal stress exceeds the maximum tensile strength of grain material. The disruption time is shorter than 60 days after the SN explosion for dust clouds located within 4 pc. The grain disruption size decreases with time at the fixed distance and increases with increasing cloud distance to the source. Strong grains (i.e., having high maximum tensile strength) are more difficult to disrupt than weak grains, and the disruption is independent of the local gas density in powerful radiation fields such as those of SNe Ia.
2. Using the grain disruption size from RATD, we model the extinction of SN light by dust grains in a nearby cloud. We find that the conversion of large grains into smaller ones by RATD results in a rapid decrease of the optical–NIR extinction but an increase in the UV extinction. This effect results in the rapid decrease of the the total-to-selective visual extinction ratio R_V over a timescale of $t_{disr} \sim 50$ days, which can successfully explain the unusually low values of R_V observed toward SNe Ia.
3. Using the RAT theory, we study the alignment of grains by SN radiation. We find that the intense SN radiation can align small grains, and the alignment size decreases with time. We model the polarization of SN light by aligned grains and find that the polarization degree increases first due to enhanced alignment by SN radiation and then drops rapidly when grain disruption begins. We find that the peak wavelength decreases rapidly from the original standard value to small values of $\lambda_{max} < 0.4\,\mu$m within less than $t_{align} < 10$ days.
4. We find that due to RATD and RAT alignment, K–λ_{max} cannot be described by the standard relationship of distant stars in the Galaxy, but it can qualitatively explain the K–λ_{max} reported for SNe Ia.
5. We suggest a possible way to constrain the cloud distance by performing very early-time observations. The time of an abrupt decrease in optical–NIR extinction and polarization would put a strong constraint on the cloud distance. An increase in the polarization degree and a decrease in the peak wavelength are also useful to test the RAT mechanism.
6. We predict an abrupt increase in the SN brightness at optical–NIR bands but a decrease in UV extinction due to RATD. This prediction can be tested with photometric and polarimetric observations at early times.
7. Our theoretical results suggest that to achieve precise measurements of cosmological distances as well as an

accurate constraint on dark energy, one needs to account for the time variation of dust extinction if dust clouds exist within several parsecs of the SN.

We thank an anonymous referee and Aleksandar Cikota for useful comments that improved our manuscript. This work was supported by the National Research Foundation of Korea (NRF) grants funded by the Korean government (MSIT) through the Basic Science Research Program (2017R1D1A1B03035359) and Mid-career Research Program (2019R1A2C1087045).

Appendix A
Grain-size Distribution Modified by RATD

In Section 3, we mentioned that there are three possible ways to calculate the grain-size redistribution function dn/da. We have shown results from model 1 where the slope is changed but the normalization constant C is constant. We now study the results for model 2 where the slope α is kept constant but the constant C changes accordingly.

With the case keeping $\alpha = -3.5$ (model 2), the new constant with the new maximum size is

$$C_{\rm new} = C\left(\frac{a_{\rm max}^{0.5} - a_{\rm min}^{0.5}}{a_{\rm disr}^{0.5} - a_{\rm min}^{0.5}}\right). \quad (28)$$

Figure 19 shows the value of α (model 1) and C (model 2) for silicate grains with time if the cloud stays at 1 pc for the different values of $S_{\rm max}$. As shown, the slope increases (i.e., becomes steeper) from the original value of $\alpha = -3.5$ to $\alpha \sim -3.62$ when RATD begins. This implies that RATD transports dust mass from large sizes to smaller sizes. The right panel shows the value of the constant normalization C which increases with time due to RATD and reaches the terminal value when RATD ceases. In general, the constant varies from $10^{-25.11}$ to 4×10^{-25} cm$^{2.5}$ with the cloud at 1 pc.

Figure 20 (left panel) shows the extinction curve after 45 days with the cloud at 0.5 and 1 pc. One can see that models 1 and 2 give similar extinction, except at optical−NIR wavelengths.

Figure 20 (right panel) shows the variation of $R_{\rm V}$ with time for the two models. Model 2 gives slightly lower extinction values than model 1 after grain disruption.

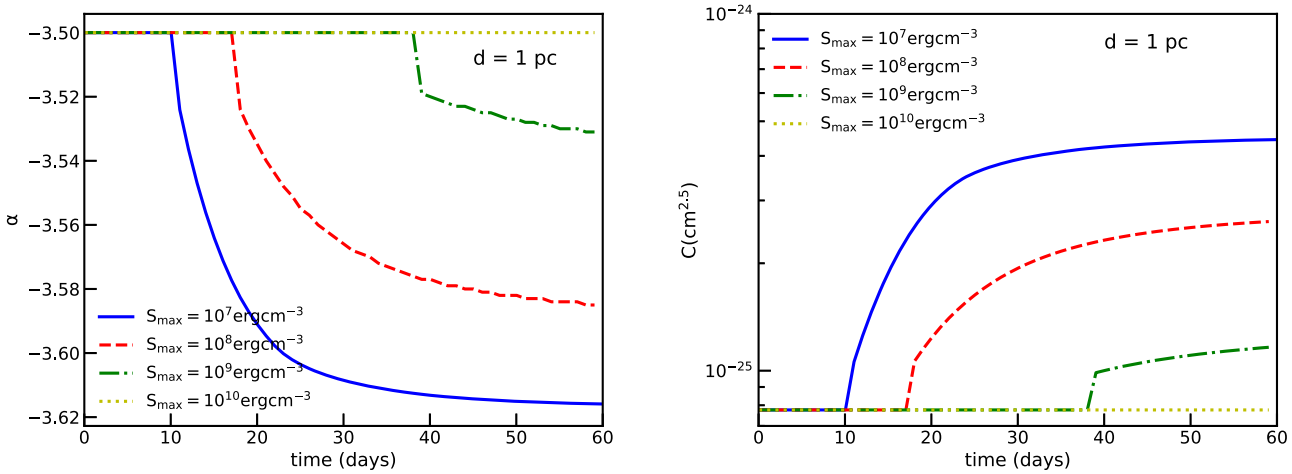

Figure 19. Variation of the slope α vs. time for model 1 (left panel) and C vs. time for model 2 for the different values of maximum tensile strength, assuming a cloud distance of 1 pc.

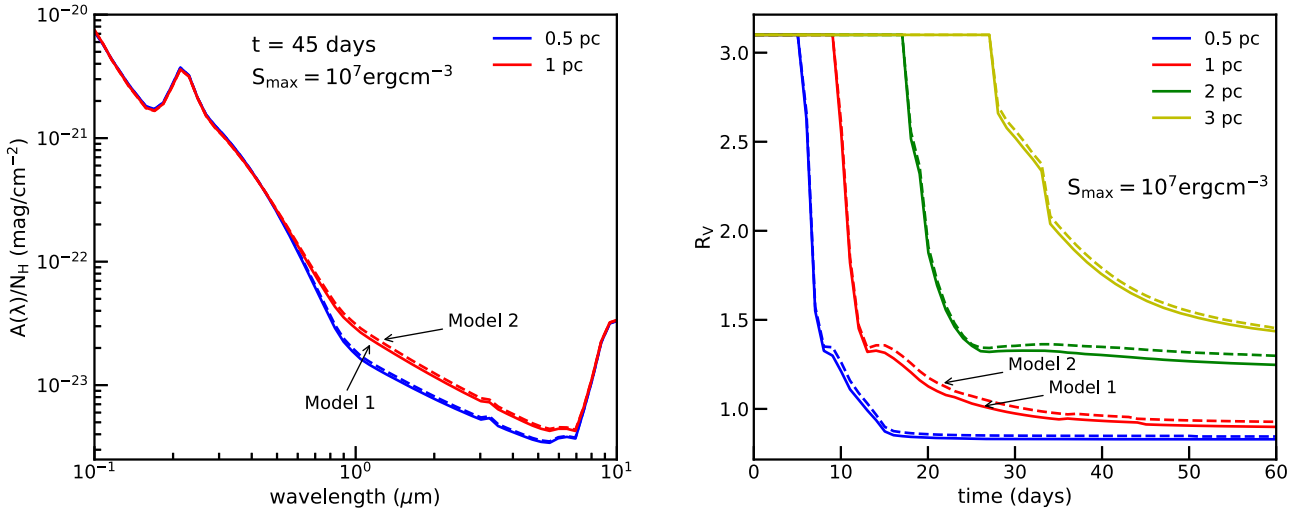

Figure 20. Left panel: extinction curve after 45 days with the cloud at 0.5 and 1 pc for model 1 (solid line) and model 2 (dashed line). Right panel: $R_{\rm V}$ vs. time for different cloud distances. The tensile strength $S_{\rm max} = 10^7$ erg cm^{-3} is assumed.

Appendix B
Observational Data of SNe Ia and Stars

Table 1 shows the physical parameters for 13 SNe Ia available in the literature.

Table 2 shows the physical parameters for 15 normal stars with low R_V but normal peak wavelength taken from Cikota et al. (2018).

Table 2
Physical Parameter for Normal Stars with Low Value of R_V, Normal λ_{max} but High K Observed by the VLT, CAHA, Asiago, and HPOL Telescopes (Cikota et al. 2018)

SN Name	Telescope	$\lambda_{max}(\mu m)$	K	R_V	$E(B-V)$
HD 54439	VLT	0.4859 ± 0.0129	0.97 ± 0.10	1.98	0.28
HD 73420	VLT	0.5465 ± 0.0175	1.04 ± 0.21	2.24	0.37
HD 78785	VLT	0.5732 ± 0.08	1.25 ± 0.01	2.29	0.76
HD 96042	VLT	0.5109 ± 0.0124	0.84 ± 0.09	1.87	0.48
HD 141318	VLT	0.5719 ± 0.017	1.19 ± 0.03	1.77	0.30
HD 152245	VLT	0.6169 ± 0.033	1.41 ± 0.07	2.02	0.42
HD 152853	VLT	0.5584 ± 0.046	1.30 ± 0.07	2.19	0.37
BD +23 3762	CAHA	0.4965 ± 0.061	0.92 ± 0.06	2.15	1.05
BD +45 3341	CAHA	0.5166 ± 0.031	1.00 ± 0.05	2.22	0.74
HD 28446	CAHA	0.4865 ± 0.076	0.70 ± 0.07	2.20	0.46
HD 194092	Asiago	0.5884 ± 0.0107	1.09 ± 0.18	2.18	0.41
HD 14357	Asiago	0.4942 ± 0.031	0.91 ± 0.04	2.12	0.56
HD 226868	HPOL	0.4425 ± 0.0262	0.57 ± 0.14	2.78	1.08
HD 218323	HPOL	0.4837 ± 0.0128	1.00 ± 0.20	2.30	0.90
HD 217035	HPOL	0.5309 ± 0.0126	0.88 ± 0.23	2.44	0.76

Appendix C
Relationship between $K-\lambda_{max}$ and $R_V-\lambda_{max}$

C.1. Fitting Polarization Curves with the Serkowski Law

We fit the theoretical polarization curves with the Serkowski law (Equation (28)) to derive the best-fit parameters K and λ_{max}, which are summarized in Table 3. Figure 21 shows the best-fit Serkowski law for the theoretical polarization curves in Figures 9 and 10 for the different times (left panel) and different cloud distances (right panel). One sees that when grain disruption and grain alignment by RATs begin, the K values increases significantly accompanied with the decrease of λ_{max}. In other words, there is a simultaneous variation in K and λ_{max} with time but they follow the opposite trend.

C.2. $K-\lambda_{max}$ and $R_V-\lambda_{max}$

To understand in more detail how K and λ_{max} change with grain disruption and alignment by RATs, we model the dust polarization by varying a_{disr} from 0.2 to 0.03 μm and a_{align} from 0.05 to 0.002 μm and derive the best-fit K and λ_{max} parameters as in the previous section.

Figure 22 (left panel) shows the resulting K–λ_{max} values. Each point represents a couple (K, λ_{max}) predicted by a given value of (a_{disr}, a_{align}). Several values of K at a given λ_{max} represents the different values of P_{max} when a_{align} decreases, and the dashed line is the best fit to these results.

In Figure 22 (right panel), we plot R_V against λ_{max} evaluated at $t = 60$ days for $S_{max} = 10^7$ erg cm^{-3} with different gas temperatures. The black solid line shows the tentative

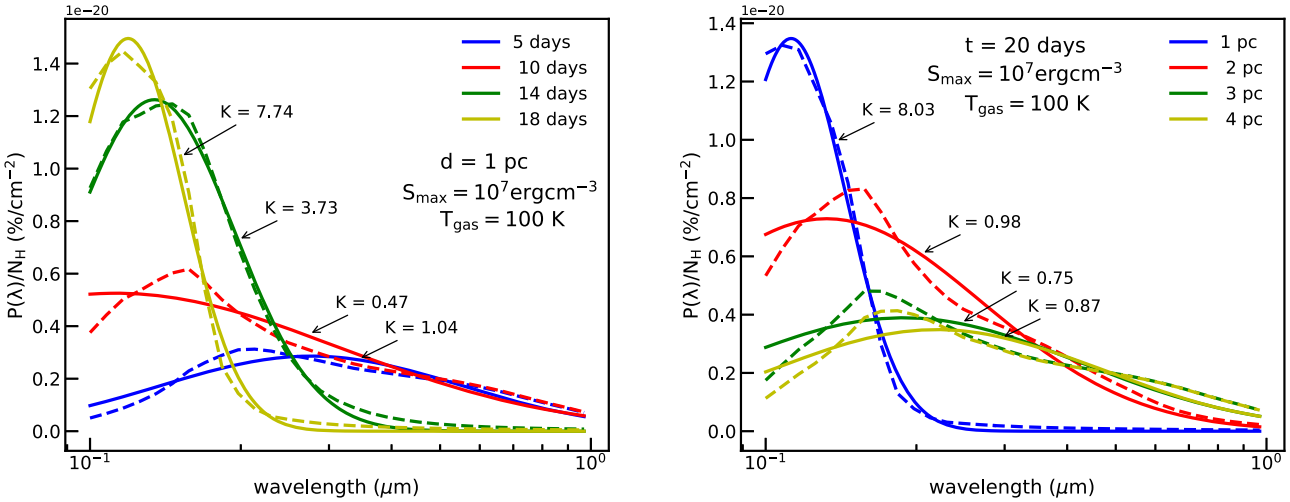

Figure 21. The best-fit Serkowski law (solid lines) for the theoretical polarization curve (dashed lines) computed at different times for a dust cloud at 1 pc in Figure 9 (left panel) and for different cloud distances at $t = 20$ days in Figure 10 (right panel).

Table 3
Model Parameters and Fitting Parameters of the Serkowski Law to the Polarization Curves Computed at Different Times for a Given Cloud Distance (Upper Table) and for Different Cloud Distances at $t = 20$ days (Lower Table)

Day	a_{align} (μm)	a_{disr} (μm)	P_{max}/N_H (%cm^{-2})	$P_{Serkowski}/N_H$ (%/cm^{-2})	λ_{max} (μm)	$\lambda_{Serkowski}$ (μm)	K
5	2.065e−2	0.250	3.125e−21	2.858e−21	0.213	0.277	1.039
10	7.227e−3	0.250	6.171e−21	5.254e−21	0.158	0.113	0.472
14	6.093e−3	0.059	12.46e−21	12.62e−21	0.146	0.134	3.728
18	5.754e−3	0.028	14.47e−21	14.95e−21	0.116	0.192	7.744

Distance (pc)	a_{align} (μm)	a_{disr} (μm)	P_{max}/N_H (%/cm^{-2})	$P_{Serkowski}/N_H$ (%/cm^{-2})	λ_{max} (μm)	$\lambda_{Serkowski}$ (μm)	K
1	5.670e−3	0.022	13.24e−21	13.47e−21	0.108	0.112	8.033
2	6.870e−3	0.143	8.314e−21	7.291e−21	0.157	0.132	0.977
3	1.164e−2	0.250	4.809e−21	3.891e−21	0.158	0.188	0.759
4	1.435e−2	0.250	4.135e−21	3.485e−21	0.183	0.220	0.869

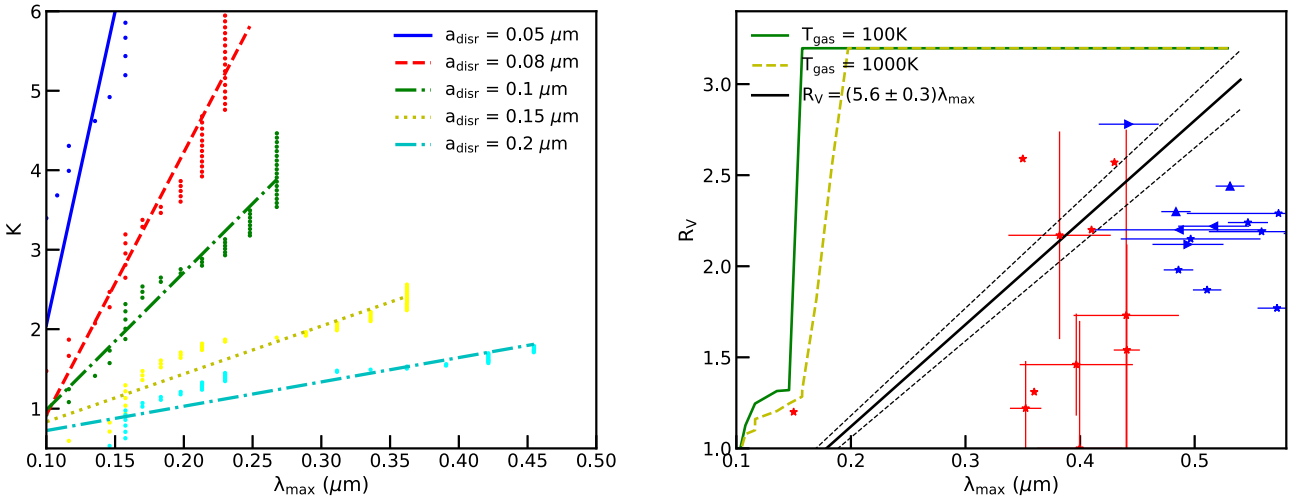

Figure 22. Left panel: K vs. λ_{max} from the best fit. Right panel: R_V vs. λ_{max} from our models overplotted with observational data for the case with different gas densities T_{gas}.

relationship reported by Whittet & van Breda (1978). As shown, both the data of SNe Ia and our modeling results do not exhibit a correlation between R_V and λ_{max}, in agreement with the finding in Cikota et al. (2018).

ORCID iDs

Thiem Hoang https://orcid.org/0000-0003-2017-0982
Le Ngoc Tram https://orcid.org/0000-0002-6488-8227

References

Amanullah, R., Goobar, A., Johansson, J., et al. 2014, ApJL, 788, L21
Amanullah, R., Johansson, J., Goobar, A., et al. 2015, MNRAS, 453, 3300
Andersson, B.-G., Lazarian, A., & Vaillancourt, J. E. 2015, ARA&A, 53, 501
Andersson, B.-G., Piirola, V., De Buizer, J., et al. 2013, ApJ, 775, 84
Arnett, W. D. 1982, ApJ, 253, 785
Brown, P. J., Smitka, M. T., Wang, L., et al. 2015, ApJ, 805, 74
Bulla, M., Goobar, A., Amanullah, R., Feindt, U., & Ferretti, R. 2018a, MNRAS, 473, 1918
Bulla, M., Goobar, A., & Dhawan, S. 2018b, MNRAS, 479, 3663
Burke, J. R., & Silk, J. 1974, ApJ, 190, 1
Burns, C. R., Stritzinger, M., Phillips, M. M., et al. 2014, ApJ, 789, 32
Chiar, J. E., Adamson, A. J., Whittet, D. C. B., et al. 2006, ApJ, 651, 268
Cikota, A., Deustua, S., & Marleau, F. 2016, ApJ, 819, 152
Cikota, A., Hoang, T., Taubenberger, S., et al. 2018, A&A, 615, A42
Cox, N. L. J., & Patat, F. 2014, A&A, 565, A61
Draine, B. T. 2003, ARA&A, 41, 241
Draine, B. T., & Lazarian, A. 1998, ApJ, 508, 157
Draine, B. T., & Li, A. 2007, ApJ, 657, 810
Draine, B. T., & Salpeter, E. E. 1979, ApJ, 231, 77
Draine, B. T., & Weingartner, J. C. 1996, ApJ, 470, 551
Foley, R. J., Fox, O. D., McCully, C., et al. 2014, MNRAS, 443, 2887
Goobar, A. 2008, ApJL, 686, L103
Herranen, J., Lazarian, A., & Hoang, T. 2019, ApJ, 878, 0
Hillebrandt, W., & Niemeyer, J. C. 2000, ARA&A, 38, 191
Hoang, T. 2017, ApJ, 836, 13
Hoang, T. 2019, ApJ, 876, 13
Hoang, T., & Lazarian, A. 2008, MNRAS, 388, 117
Hoang, T., & Lazarian, A. 2009, ApJ, 695, 1457
Hoang, T., & Lazarian, A. 2014, MNRAS, 438, 680
Hoang, T., & Lazarian, A. 2016, ApJ, 831, 159
Hoang, T., Lazarian, A., & Martin, P. G. 2013, ApJ, 779, 152
Hoang, T., Lazarian, A., & Martin, P. G. 2014, ApJ, 790, 6
Hoang, T., Tram, L. N., Lee, H., & Ahn, S.-H. 2019, NatAs, 3, 766
Hough, J. H., Bailey, J. A., Rouse, M. F., & Whittet, D. C. B. 1987, MNRAS, 227, 1P
Kawabata, K. S., Akitaya, H., Yamanaka, M., et al. 2014, ApJL, 795, L4
Lazarian, A., Andersson, B.-G., & Hoang, T. 2015, in Polarimetry of Stars and Planetary Systems, ed. L. Kolokolova, J. Hough, & A.-C. Levasseur-Regourd (New York: Cambridge Univ. Press), 81
Lazarian, A., & Hoang, T. 2007, MNRAS, 378, 910
Lazarian, A., & Hoang, T. 2019, ApJ, 883, 122
Li, A., & Draine, B. T. 2001, ApJ, 554, 778
Mathis, J. S., Rumpl, W., & Nordsieck, K. H. 1977, ApJ, 217, 425
Nobili, S., & Goobar, A. 2008, A&A, 487, 19
Patat, F., Baade, D., Höflich, P., et al. 2009, A&A, 508, 229
Patat, F., Taubenberger, S., Cox, N. L. J., et al. 2015, A&A, 577, A53
Phillips, M. M., Simon, J. D., Morrell, N., et al. 2013, ApJ, 779, 38
Riess, A. G., Filippenko, A. V., Challis, P., et al. 1998, ApJ, 116, 1009
Riess, A. G., Filippenko, A. V., Li, W., et al. 1999, ApJ, 118, 2675
Scolnic, D., Perlmutter, S., Aldering, G., et al. 2019, arXiv:1903.05128
Serkowski, K., Mathewson, D. S., & Ford, V. L. 1975, ApJ, 196, 261
Wang, X., Li, W., Filippenko, A. V., et al. 2008, ApJ, 677, 1060
Wang, X., Wang, L., Filippenko, A. V., et al. 2012, ApJ, 749, 126
Waxman, E., & Draine, B. T. 2000, ApJ, 537, 796
Weingartner, J. C., & Draine, B. T. 2001, ApJ, 548, 296
Whittet, D. C. B., Duley, W. W., & Martin, P. G. 1990, MNRAS, 244, 427
Whittet, D. C. B., Martin, P. G., Hough, J. H., et al. 1992, ApJ, 386, 562
Whittet, D. C. B., & van Breda, I. G. 1978, A&A, 66, 57
Wilking, B. A., Lebofsky, M. J., Martin, P. G., Rieke, G. H., & Kemp, J. C. 1980, ApJ, 235, 905
Zelaya, P., Clocchiatti, A., Baade, D., et al. 2017, ApJ, 836, 88
Zheng, W., Kelly, P. L., & Filippenko, A. V. 2017, ApJ, 848, 66